UNIVERSITY OF OKLAHOMA

GRADUATE COLLEGE

GOES-R STEREOSCOPIC CLOUD TOP RETRIEVAL ALGORITHM USING NORMALIZED CROSS-CORRELATION FOR 1-MIN OVERSHOOT ANALYSIS

A THESIS

SUBMITTED TO THE GRADUATE FACULTY

in partial fulfillment of the requirements for the

Degree of

MASTER OF SCIENCE IN METEOROLOGY

By

TYLER YOUNG
Norman, Oklahoma
2021

Downloaded from SHAREOK. Persistent Handle URL: https://hdl.handle.net/11244/330215

GOES-R STEREOSCOPIC CLOUD TOP RETRIEVAL ALGORITHM USING NORMALIZED CROSS-CORRELATION FOR 1-MIN OVERSHOOT ANALYSIS

A THESIS APPROVED FOR THE
SCHOOL OF METEOROLOGY

BY THE COMMITTEE CONSISTING OF

Dr. Cameron R. Homeyer, Chair

Dr. Kristin M. Calhoun

Dr. Pierre E. Kirstetter

© Copyright by TYLER YOUNG 2021
All Rights Reserved.

Acknowledgments

This work was completed with the help of several colleagues. The author would like to thank the thesis committee for their feedback and support. I would like to thank Dr. Homeyer for his guidance, mentorship, and time spent teaching and editing all of the work done. Further, my family and friends deserve to be recognized for their support throughout this process. The author also thanks other members of the Convection, Chemistry, and Climate research group for their support. Finally, the author would like to thank the NOAA Satellite Analysis Branch for approving multiple research requests for overlapping mesoscale domains from GOES-16 and GOES-17. This work was supported by the National Aeronautics and Space Administration (NASA) under Award 80NSSC19K0347.

Table of Contents

Acknowledgments **iv**

List of Tables **vi**

List of Figures **vii**

Abstract **ix**

1 Introduction **1**
1.1 The Importance of Overshooting Tops 1
1.2 History of Stereoscopy in Meteorology 3
1.3 Thesis Goals and Hypotheses 7

2 Data and Methods **9**
2.1 Satellite 9
2.2 Radar 10
2.3 Tropopause 10
2.4 Stereoscopy Algorithm 11

3 Results and Discussion **22**
3.1 Case Studies 22
3.2 Limitations of Stereoscopy Algorithm 35

4 Summary and Conclusions **42**

Reference List **45**

List of Tables

3.1 Table describing all cases included in this study. Cases which were requested through the Satellite Analysis Branch are bolded. 22

List of Figures

2.1 Raw (left), regridded (middle), and rebinned (right) imagery from GOES-16 on 22 May 2020 valid at 2340 UTC. 12

2.2 Technique used to match GOES images. A template centered at x_0,y is compared to the same size neighborhood from GOES-17 centered at x_0,y and shifted the length of the search area to find best match. . . . 14

2.3 Illustration of the Iterative Process. For each iteration the template size and search area are decreased. 16

2.4 Raw disparity values (left) and filtered disparity values (right) after 4 iterations are shaded in blue from 22 May 2020 valid at 2340 UTC. . 18

3.1 Selected storm track origins (stars) and NEXRAD WSR-88D vertical sampling in VCP-11 mode of the 0-20 km ASL altitude layer. 23

3.2 History maps from 17 May 2019 of a.) maximum 20 dBZ echo top height b.) maximum stereo c.) 20 dBZ echo top tropopause relative height d.) stereo tropopause relative height e) maximum reflectivity f) minimum IR temperature. 25

3.3 Time series analysis of stereo height (red), 20 dBZ echo top height (blue) and error (dashed blue), and tropopause height (black) of storm tracks 2 and 5 from 17 May 2019, identified by the storm tracking algorithm. Error bars are 1.25 km and 1 km for Track 2 and 5, respectively. These error bars are extracted from the 0-20 km average vertical sampling from GridRad shown in Figure 3.1. 27

3.4 As in Fig. 3.2, but for 13 May 2020. 30

3.5 As in Fig. 3.3, but for tracks 18, 30 and 69 from 13 May 2020. Error bars are 1.75 km, 0.5 km, and 1.5 km, respectively. 31

3.6 As in Fig. 3.2, but for 22 May 2020. 32
3.7 As in Fig. 3.3, but for tracks 12 and 14 from 22 May 2020. Error bars are 0.75 km for both tracks. 33
3.8 As in Fig. 3.2, but for 8 June 2020 34
3.9 As in Fig. 3.3, but for tracks 13 and 15 from 8 June 2020. Error bars are 1 km for both tracks. 35
3.10 As in Fig. 3.2, but for 6 April 2021. 36
3.11 As in Fig. 3.3, but for tracks 7 and 9 from 6 April 2021. Error bars are 0.75 km for both tracks. 37
3.12 As in Fig. 3.2, but for 23 April 2021. 38
3.13 As in Fig. 3.3, but for track 34 from 23 April 2021. Error bar is 0.5 km. 39
3.14 Aggregate of the difference in stereo heights and 20 dBZ echo top heights (left) and 10 dBZ echo top heights (right) from storm tracks presented in this study. 40
3.15 Zoom in of overshoot from a.) GOES-16 and b.) GOES-17 from 22 May 2020 valid at 2340 UTC. 41

Abstract

Satellite-based cloud top height (CTH) analyses are instrumental in understanding storm dynamics which can be utilized for severe and tornado warnings. Currently, CTHs are derived using IR imagery which are subject to errors. Some assumptions used when determining CTHs solely from IR produce less reliable CTHs such as knowledge of cloud emissivity, ambient temperature, lapse rate, and that the cloud is in thermodynamic equilibrium which is least true around intense thunderstorms. A method proposed for obtaining more accurate CTHs is stereoscopy since it is dependent on geometric relationships. Stereoscopy is a scientific technique used to combine two images to enhance the illusion of depth. This technique can be applied to weather phenomena using visible or infrared satellite images to retrieve CTHs. GOES-16 and GOES-17 mesoscale sector scans are time synchronized and can be used to take images of the same field of view with different viewing points. Conducting stereoscopy on this data can ultimately determine an offset between the two GOES images which is proportional to the corresponding CTH. Previous stereoscopy studies to calculate CTHs using American satellites have been conducted on thunderstorms and hurricanes in the 1980's and 1990's. Since then, satellites have advanced and the spatial and temporal resolution of visible and infrared images from new-era GOES are now available at 0.5 km and 2 km resolution, respectively, every minute. It is hypothesized this increase in resolution will allow cloud height calculations accurate to within 500 m which is higher than the accuracy found in past studies of 1500 m. Retrieved CTHs are compared to echo top heights from GridRad to determine validity of the height estimate. The nature of analyzing storms through stereoscopy presents several constraints. Visible imagery from GOES constrains analyses to storms during the day. In addition, using GOES-16 and GOES-17 as the two satellites only allows for analyses of storms over the central U.S. since it is where both mesoscale floating

domains overlap. These CTH analyses alongside radar data and storm reports can be used to further investigate severe storm dynamics.

Chapter 1

Introduction

1.1 The Importance of Overshooting Tops

The Great Plains are home to some of the most severe thunderstorms in the world. These storms are driven by intense updrafts, with the strongest often penetrating the tropopause. Deep convection exists around the world but storms that penetrate the tropopause are most common in the mid latitudes within an environment of lower tropopause heights. Storms that penetrate the tropopause are identified by locating overshooting tops (OT). An overshooting top is a cloud feature located above the anvil cloud and occurs when a rising air parcel penetrates past its level of neutral buoyancy. Cloud top heights (CTH) of the most intense OTs can reach over 20 km. In addition, some OTs can produce above-anvil cirrus plumes (AACPs). AACPs are often produced in storm-relative wind environments favoring gravity wave breaking and typically appear warmer in infrared imagery as the cirrus cloud adjusts to the temperature of the lower stratosphere (Bedka et al., 2018). Bedka et al. (2015) have shown the identification of these features, in some situations, can provide increased warning time of potential severe weather with an average lead time of 18 minutes.

It was found by Adler and Fenn (1981) that CTHs ascend above the tropopause 30-45 minutes before a tornado forms and stays constant or decreases slightly as the tornado is ongoing. However, using infrared satellite, Sandmæl et al. (2019) illustrated there was little to no correlation between colder cloud top temperatures to distinguish between non-severe and severe storms. Nonetheless, cloud top height information along with overshooting top growth rates has potential to be used in an operational setting to improve upon lead time for tornado warnings. OTs are also indicative of strong updrafts capable of producing large severe hail. The longer and

higher hail embryos can be suspended in the middle troposphere, the more they can grow and then fall as large hail.

In addition to severe weather, OTs are important for understanding atmospheric chemistry and composition of the upper troposphere and lower stratosphere (UTLS) since OTs are a vehicle for transporting lower tropospheric material to this region. The chemistry, dynamics, and radiative properties of the UTLS can be heavily impacted by transported trace gases (e.g., Gettelman et al., 2011; Holton et al., 1995; Stohl et al., 2003). Water vapor, ozone, and carbon monoxide are among a few important gases impacted by convection in the UTLS. Particularly, greenhouse gases are important when considering the impact on the radiative transfer process. The residence times of trace gases in the UTLS vary depending on species and the height at which air was lofted to. Material penetrating into the stratospheric overworld (>380K level, typically 3+ km above the tropopause in midlatitudes) will have a longer stratospheric residence time than material lifted only 1-2 km above the tropopause (the lowermost stratosphere in midlatitudes). In addition, upper-level circulations such as the quasi-stationary anticyclone over North America in the summer can regionally trap convective material lofted to the lower stratosphere (Cooney et al., 2018).

Several studies have attempted to accurately quantify overshoot occurrences in the U.S. However, a large false detection rate was common across satellite based methods using both visible and IR imagery from a single satellite from previous GOES generations. Studies conducted by Berendes et al. (2008), Lindsey and Grasso (2008), and Rosenfeld et al. (2008) used visible and near-infrared algorithms to detect storms penetrating the tropopause. Methods that rely on visible imagery are limited to daylight detection and are less reliable at large solar zenith angle time periods such as sunrise and sunset due to the enhanced texture. Since the majority of OTs occur at night (60%-75%; Bedka et al., 2010), the larger concern is the inability of these methods to detect OTs at night. In addition, these methods fail to account for

tropopause modification from convection. Bedka et al. (2010) proposed an alternative method using IR brightness temperature and the temperature of the tropopause. A threshold of 6.5 K colder than the surrounding environment was set to categorize a point as penetrating the tropopause. However, because IR profiles and cloud top heights do not have a completely direct relationship due to radiative processes, this method can have up to a 38.8% false detection rate (Bedka et al., 2010). In contrast to employing satellite based data to detect OTs, Solomon et al. (2016) used three-dimensional gridded NEXRAD data, referred to as GridRad which is explained in Section 2.2., to compare 10 dBZ echo top heights to tropopause heights at 3 hour intervals in a 5 year study. To build upon and further improve this method through increasing the temporal resolution, Cooney et al. (2018) conducted a 10 year study at hourly intervals using the same GridRad data set. With the goal of obtaining more accurate CTH calculations, stereoscopic analysis of GOES imagery is utilized to detect overshoots in the Central Plains, which is the most common region for overshoots to occur (Cooney et al., 2018).

1.2 History of Stereoscopy in Meteorology

The use of photogrammetry to calculate the height of clouds has a long history. In the 1920's, ground-based cameras and eventually vertically-looking cameras from high altitude planes were used to measure cloud characteristics. The first quantitative work involving ground-based photography was not until Meyer in 1954 (Meyer, 1954) and Kassander and Sims in 1957 (Kassander and Sims, 1957). The aerial photographs from high flying aircraft were most similar to satellite images used today for stereoscopy. An example of this would be using a high-altitude surveillance aircraft flying at 20 km to take photographs, similar to what Roach did in 1967 (Roach, 1967). The first documented case of stereoscopy from a satellite was in 1966 when Ondrejka and Conover used the vidicon tube weather satellites. Specifically, they took two images

approximately 3 minutes apart from NASA's polar-orbiting Nimbus II APT which yielded CTH accuracies within 2 km (Ondrejka and Conover, 1966). In 1968, Kikuchi and Kasai used the same satellite to distinguish between sea ice and clouds and allocate clouds into 3 layers (Kikuchi and Kasai, 1968). However, the resolution on the Nimbus 2 APT was as coarse as 3 km, leading to larger inaccuracies when calculating CTH. Other polar orbiting satellites such as Apollo and Skylab were able to produce higher quality imagery and therefore more accurate calculations were possible. The higher quality stereo was demonstrated by Shenk et al. (1975) when observing the cloud structure associated with a cold front through Apollo 6, and Black who viewed hurricanes through Skylab (Hasler, 1981).

Past stereoscopic studies included a combination of Low Earth Orbiting (LEO) satellites and Geosynchronous Earth Orbiting (GEO). Data over the same domain for LEO and GEO satellites is less common than pure GEO stereo since LEO passes over the GEO domain are limited. Due to the constant orbiting of the earth about the poles, a given LEO satellite is only viewing a certain region for a short period of time. Polar-orbiting satellites have limitations on their use for stereoscopy but have also proven reliable when paired with GEO systems. Stereoscopy requires two views of the same region over a period of time which a single polar-orbiting satellite does not fulfill. This led Shenk and Bristor and Pichel (Hasler et al., 1983) to propose using GEO satellites to conduct stereoscopy. In May 1974 and February 1975, SMS-1 and SMS-2 were launched respectively. The two satellites provided a spatial resolution of 1 km while being stationed at 75° W and 107° W creating 32 degrees of separation allowing a cloud field to be viewed at drastically different angles. Minzner et al. (1978) were the first to use two GEO satellites to show quantitative stereoscopy height calculations. These calculations within a 2-sigma uncertainty were accurate to 0.5 km and maps of 5 km contours were able to be created (Minzner et al., 1978). In the same year two scientists, Bryson and desJardins, worked independently to create

processing techniques to remap the stereo images digitally. The technique developed by desJardins was conducted at the Goddard Space Flight Center (GSFC) on the Atmospheric and Oceanic Information Processing System (AOIPS; Hasler, 1981). On 26 May 1978 the National Oceanic and Atmospheric Administration (NOAA) ran the first synchronized scans of GOES-E and GOES-W. To ensure quality, high altitude lakes were used to determine the accuracy of the stereoscopic cloud top heights from the synchronized GOES scans. Furthermore, during the Spring of 1979 the first scan synchronous short interval GOES images of severe thunderstorms occurred during the SESAME field campaign (Alberty et al., 1979). Lastly, in the fall of the same year, the first short interval GOES images of a tropical cyclone were taken during Hurricane Frederic.

There are several characteristics the satellites being used for stereoscopic analysis must meet. According to Hasler (1981), in order to obtain accurate stereo, the scan from the two satellites must be within 30 seconds of each other because convective clouds change rapidly and matching features in time-spaced scans can be impossible in such cases. An earlier study using two European satellites, Meteosat-5 and Meteosat-8, had a 15-minute difference between scans of the same domain. To account for this, Seiz et al. (2007) assumed no vertical motion and constant winds to interpolate cloud heights at a specified time to account for this error. While this may allow for accurate calculations for non-convective clouds, the assumptions used are easily violated in the presence of convection and OTs.

While a majority of the early studies using stereoscopy used American satellites, more recent studies used satellites across the globe including Asia and Europe. In 1980 the Japanese Geosynchronous Satellite and GOES-W were synchronized to observe the Central Pacific. Combinations of satellites with different spatial resolutions, temporal resolutions, and longitudinal separation were compared to examine the sensitivities of these factors (Lee et al., 2020). A large longitudinal separation between

satellites is ideal to increase contrast between the images and to capture parts of the cloud that the other satellite would not be able to observe because of cloud slopes and shadows. The only drawback to a larger longitudinal separation between satellites is the data on the fringes of images will be at a lower resolution. The lower resolution and blur that results make it harder for accurate stereo matches to be obtained. Another limitation to using visible imagery is the temporal coverage of data only during the day. The incorporation of IR images was explored to create IR stereo to account for the poor temporal extent of visible imagery. IR stereo is not quantitatively as accurate as visible due to the coarsened resolution and cloud emissivity. In addition to visible and IR stereo techniques, Hasler (1981) briefly proposed a synthetic option using visible and IR to create artificial stereo images.

Prior to Hasler et al. (1991) stereoscopic analysis was done through a binocular viewer of a stereo image pair. AOIPS/2 was used for preprocessing satellite images before viewing through the lens and conducting stereo analysis. The process of matching cloud features through this method would take several hours. A 512x512 pixel image from the 1980's has roughly 16 times fewer pixels than the 2000x2000 pixel image from current GOES satellites. Taking into consideration the higher resolution of modern GOES imagery, the same method would likely take several days. Hasler et al. (1991) proposed an automatic stereo method using a massively parallel processor computer to carry out the nearly 100 billion calculations required for a 512x512 pixel image.

The possibilities of stereoscopy extend beyond CTH calculations. Stereoscopic analysis can also reveal the height of volcanic ash plumes, wildfire smoke, and dust. Hasler et al. (1983) outlines some potential applications of meteorological stereoscopy which includes cloud top and base height measurements, cloud-wind height assignment, vertical motion estimates for convection, temperature vs. height measurements when paired with infrared observations, and cloud emissivity measurements.

1.3 Thesis Goals and Hypotheses

Most current single-satellite methods for retrieving CTH rely on IR measurements. Such methods are most inaccurate when CTHs reach above the tropopause as the cloud tops either continue to cool or mix with the surrounding environment producing a cloud top temperature (CTT) reading which, when matched with the tropospheric temperature profile (as is common), is not representative of its true height. Using IR to calculate CTHs requires knowledge of cloud emissivity, ambient temperature, lapse rate, and the assumption that the cloud is in thermodynamic equilibrium which is least valid around intense thunderstorms (Hasler, 1981). Setvák et al. (2013) showed utilizing satellite observations there is no direct link between IR temperature and CTH. This was most evident in areas of enhanced-V signatures from IR imagery. However, Griffin et al. (2016) leveraged the brightness temperature difference from the OT and anvil region and NWP-derived height differences to find a mean lapse rate for the overshooting depth. Since anvil heights are usually well known, Griffin et al. (2016) was able to calculate OT heights based off of this assumed linear relationship. It was found these heights were within 500 m of 75% of MODIS and 65% of GOES OT heights when compared to CloudSat's cloud profiling radar (CPR) estimated heights. This thesis develops methods to apply stereoscopy to modern GOES imagery, which as a concept is a more reliable method to retrieve CTH. Stereoscopy applies geometric relationships to visible images from two or more satellites viewing the same domain to derive CTHs.

Applying stereoscopic analysis to meteorological data has proved to be advantageous in calculating the CTH of both severe thunderstorms and hurricanes. For this study, a cloud top height retrieval algorithm using 1 minute GOES-16 and GOES-17 visible and IR images will be used to retrieve CTHs. The floating mesoscale domains of each satellite are utilized to provide high temporal resolution (30-s to 1-min) for

storms over the Central United States. This is where storms most commonly overshoot the tropopause as well as where both floating mesoscale domains from the satellites can overlap. With a spatial resolution of 0.5 km for visible images, it is hypothesized a CTH accuracy of at least 0.5 km is achievable. Radar echo top heights and tropopause heights will be used as comparisons to the CTHs calculated from the stereoscopic analyses. The novelty of 1-min GOES imagery allows one to resolve the finer time scale pulses of OTs that 5-min GOES imagery and radar volumes can not. The magnitude and rapidness of these pulses can be seen through an IR time series analysis from Figure 15 in Bluestein et al. (2019). Also, alternative data sets can not resolve the finer temporal scale features examined in Fujita (1974) shown in Table 1, which on average display 5 minute cycles. Being able to resolve these finer scale processes can be used in UTLS transport analyses to learn about stratospheric composition ramifications and severe weather nowcasting. The evolution of OTs and possible lag in time from OT pulse to severe weather can be examined in this higher temporal resolution data.

Chapter 2

Data and Methods

2.1 Satellite

Geostationary Operational Environmental Satellite (GOES) visible and IR imagery was obtained through NOAA's Comprehensive Large Array-data Stewardship System (CLASS; NOAA, 1994). Operational GOES consists of GOES-East and GOES-West which are both stationed over the equator at 75° W and 135° W longitude, respectively. For all time periods analyzed in this study GOES-16 is in the east position and GOES-17 is in the west position. GOES-16 and GOES-17 provide imagery at 5-minute intervals over the Contiguous United States (CONUS) and at 1-minute intervals over a smaller floating mesoscale domain which each satellite has two of. This study will use data from the Advanced Baseline Imager (ABI) using the 1-minute mesoscale domains, for cases when the domains from GOES-16 and GOES-17 overlap. From these mesoscale floaters the raw data is not used, but instead 2 of the 16 bands ABI has to offer which consists of 2 visible, 4 near-IR, and 10 IR bands, were selected. Band 2 and Band 14 from the ABI are used for adjusted visible and IR imagery respectively. Band 2, the "red" band, uses a wavelength of 0.64 micometers and captures visible imagery at a horizontal resolution of 0.5 km. Band 14, the IR longwave band, uses a wavelength of 11.2 micrometers and has a horizontal resolution of 2 km (Schmit et al., 2012). Band 2 was chosen because it provides the highest resolution of visible imagery and Band 14 was chosen because it is most similar to standard longwave IR imagery used for CTH and CTT. Although 4 events were successfully requested through the Satellite Analysis Branch, 2 were excluded from this study for unsatisfactory storm initiation.

2.2 Radar

Comparisons of stereo CTH and radar data are made in this study. Gridded NEXRAD Weather Surveillance Radar-1988 Doppler (WSR-88D) data, or GridRad, is a three-dimensional merged multi-radar data volume that allows for detailed geometric overshooting analyses over the CONUS (Homeyer and Bowman, 2017). GridRad merges individual radar volumes using space- and time- weighted binning (averaging) of observations, limiting contributions from individual radars to 300 km in range from the radar location and up to 5 minutes removed from the analysis time. Here, version 4.2 of the GridRad algorithm is used to create volumes of radar reflectivity at $\sim$0.02° longitude-latitude resolution ($\sim$2-km) and 0.5-1 km altitude resolution up to 22 km above sea level (0.5 km in the lowest 7 km above sea level, 1 km otherwise) and at 5-minute time intervals. The data quality controls discussed in (Homeyer and Bowman, 2017) were applied.

2.3 Tropopause

The newest reanalysis data produced by the NASA Global Modeling and Assimilation Office (GMAO) is the second Modern-Era Retrospective analysis for Research and Applications (MERRA-2; Gelaro et al., 2017). This newer reanalysis replaced MERRA with upgrades including the newest version of the Goddard Earth Observing System Model, Version 5 (GEOS-5) data assimilation system, the ability to assimilate more observations, and a slightly higher resolution in the horizontal. MERRA-2 outputs data with a horizontal resolution of 0.625° x 0.5° (lon x lat) and a temporal resolution of 3 hours. Tropopause heights were calculated based on the World Meteorological Organization lapse-rate definition and are used to determine overshooting top events (WMO, 1957). The tropopause data is linearly interpolated in space and time from the MERRA-2 grid to the finer GridRad and stereo grids.

2.4 Stereoscopy Algorithm

Since stereoscopic analysis was first used for meteorological studies, scientists have continued to propose improvements for conducting stereo. Each method has been unique and this research will also propose new processes. However, the basic framework used for the CTH retrieval algorithm follows that originally outlined in Hasler et al. (1991).

Two geostationary satellites, GOES-16 and GOES-17, are used as the two storm-top perspectives in the central U.S. As documented previously, bands 2 and 14 from the ABI will be used for visible and IR imagery. While IR stereo will not be conducted in this study, IR imagery will be used for quality control.

The steps of our CTH retrieval algorithm are as follows:

1. Preprocessing and Regridding

   Previous studies have used methods of image enhancement, normalization, and de-striping to maximize the signal-to-noise ratio in the image matching process. However, because GOES-16 and GOES-17 have upgraded imaging capabilities compared to previous generations of satellites, it was found that normalizing and enhancing the images beyond the products used did not lead to improved matching performance. Matching the images is how the spatial offset, or disparity, is determined between unique features within the image. The disparity value is proportional to the CTH.

   Since the earth has a curved surface and each satellite has a different viewing angle, the images will be distorted, most extreme near observational edges. For accurate feature matching the images need to be regridded to a common domain. The GOES data from GOES-16 and GOES-17 are regridded so they are both on the same regular latitude and longitude grid. Satellite domains for the cases presented will either have the same center point or differing center points (which

would yield a smaller overlapping region). To account for this, a filter is applied so data points only pass through to analysis if they fall within the overlapping domain. Raw images of the mesoscale domains contain 2000x2000 pixels and, due to the curvature of the Earth, viewing angles, and domain filter, the ending stereo image will be smaller.

Unlike several past studies, since both satellites are time synchronized with differences less than 30 s, for every timestep of our reference satellite, chosen to be GOES-16, there is a paired image from the test satellite, GOES-17. Thus, images do not need to be interpolated to correct for a larger time difference like older satellites with a coarser time resolution. GOES-16 was chosen as the reference satellite since it is at less of an angle to the central U.S (and thus, provides the finest image quality) which is the target region for conducting stereo. This means all disparity values calculated will be in reference and comparable to the GOES-16 image.

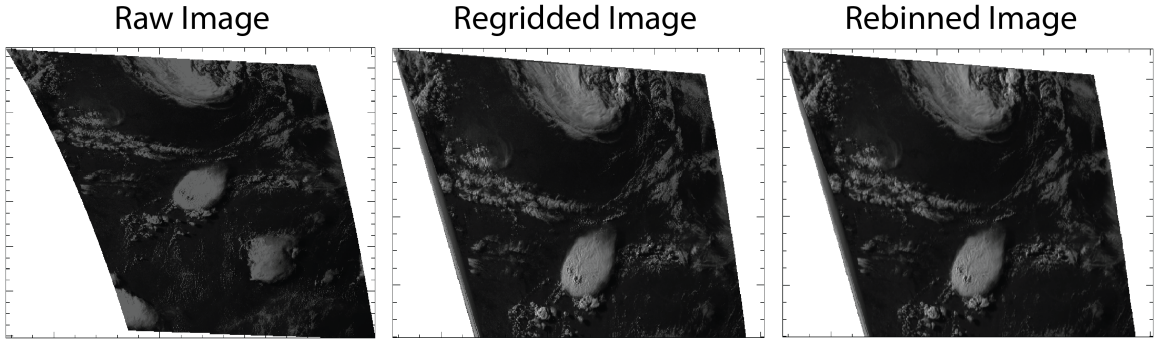

Figure 2.1: Raw (left), regridded (middle), and rebinned (right) imagery from GOES-16 on 22 May 2020 valid at 2340 UTC.

With the higher temporal and spatial resolution of the new-era GOES, this process is dramatically more computationally expensive compared to previous studies. A higher computational time is not ideal for the algorithm to be ultimately useful in an operational setting. Due to this higher resolution a solution

to decrease the time needed to process and calculate CTHs needed to be explored. It was found by rebinning the visible image array into a coarsened image for the initial large-area matching steps that the computational time was decreased exponentially with no change in the performance of the algorithm. Rebinning "minifies" the visible imagery using neighborhood averaging to create an array with dimensions smaller by a set factor.

2. Image Matching

   The matching step ultimately assigns a disparity value to each pixel in the GOES-17 image in respect to the reference image, GOES-16. In terms of the x-y grid, since GOES-17 projects clouds to the east and GOES-16 projects clouds to the west (so-called "parallax" displacement from objects residing at altitudes above the Earth surface), GOES-17 pixels must be moved west, or in the negative x-direction, to match the reference image. This means the disparity value will be negative in the x-direction. For simplicity, the disparity value will be referred to in terms of its magnitude. With GEO/LEO stereo the latitudinal parallax would need to be taken into account due to the different positions in latitude of the satellites. However, for GOES-16 and GOES-17 a simple comparison of differences in parallax calculation for the two satellites shows the resulting differences in latitude parallax are minuscule. Therefore, the parallax only needs to be calculated in the longitudinal direction.

   To assign a disparity value a match score is performed for each pixel in the test image. To do this a method employing templates and search areas is used. A match score is not computed between 1 pixel, a 0.5 km x 0.5 km area, from GOES-17 and 1 pixel in GOES-16, but instead a template (or multi-pixel neighborhood) from GOES-17 and a neighborhood from GOES-16. A template refers to the surrounding pixels from a center point in GOES-17 being compared to a center point and a neighborhood in the surrounding pixels of the center point

from GOES-16. For each point in the test image the corresponding template is compared to several neighborhoods within the reference image to find the best match. The neighborhoods being considered composes the search area (varying east-west in this case). The center of the search area is the same x-y coordinate as the reference image center pixel as shown in Figure 2.2.

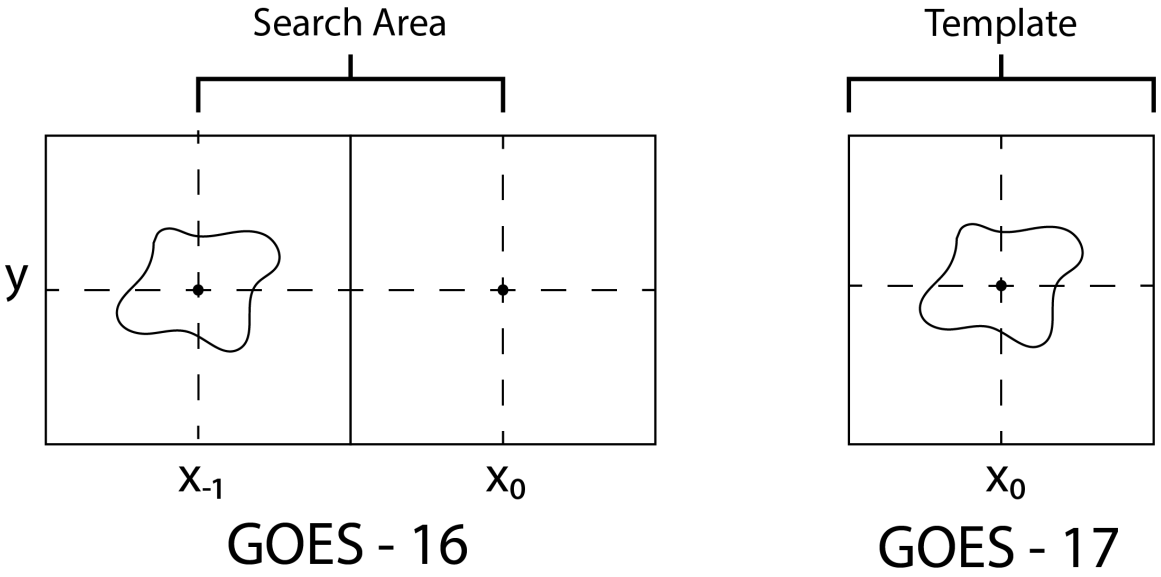

Figure 2.2: Technique used to match GOES images. A template centered at x_0,y is compared to the same size neighborhood from GOES-17 centered at x_0,y and shifted the length of the search area to find best match.

The best match is the paired template and neighborhood that has the highest match score. The match score (k) is the normalized mean and covariance correlation shown in Equation 2.1.

$$k = \frac{\sum(x_i - \bar{x})(y_{i-k} - \bar{y}_k)}{[\sum(x_i - \bar{x})^2]^{\frac{1}{2}}[\sum(y_{i-k} - \bar{y}_k)^2]^{\frac{1}{2}}} \tag{2.1}$$

where x_i is the grey level of the ith pixels in the template, y_{i-k} is the grey level of the ith pixels and kth search area in the neighborhood, $\bar{x}$ is the mean value over the template, and $\bar{y}_k$ is the mean value over the neighbor hood for the kth search area.

The disparity value is then set as the difference between the center pixel of the matching neighborhood and the original starting center pixel of the search area where the match score is maximized. This process is done for every pixel in the reference image. The end result is an array of disparity values which can then be used to calculate the CTH at every pixel since the disparity is proportional to CTH. However, to more accurately calculate a disparity value, this process is repeated with each iteration shrinking the template sizes and search areas to refine the initial matches to be sensitive to smaller-scale features (e.g., overshoots).

3. Iterative Process

To match cloud features at the smallest scale the template and search areas need to be on the order of kilometers. However, starting off with smaller template sizes will create too much error and noise for any filtering and smoothing to overcome. In addition, using template sizes on the order of tens of kilometers will not be able to accurately match smaller cloud features such as overshooting tops. An iterative process is employed to combat this problem. Four iterations, with each subsequent template and search area getting smaller, will first match the broader cloud field and then resolve smaller features with each step. For each case the first iteration's search area is either 64 or 80 pixels. These were manually determined based on the maximum CTH for each event. This presents a downside in this algorithm for the first iteration's search area having to be chosen for each case. It was determined that too high of an initial search area allowed the matching process to stray too far from plausible matches when

the maximum CTH was relatively low. Figure 2 shows the dimensions of the template size and search area for each iteration.

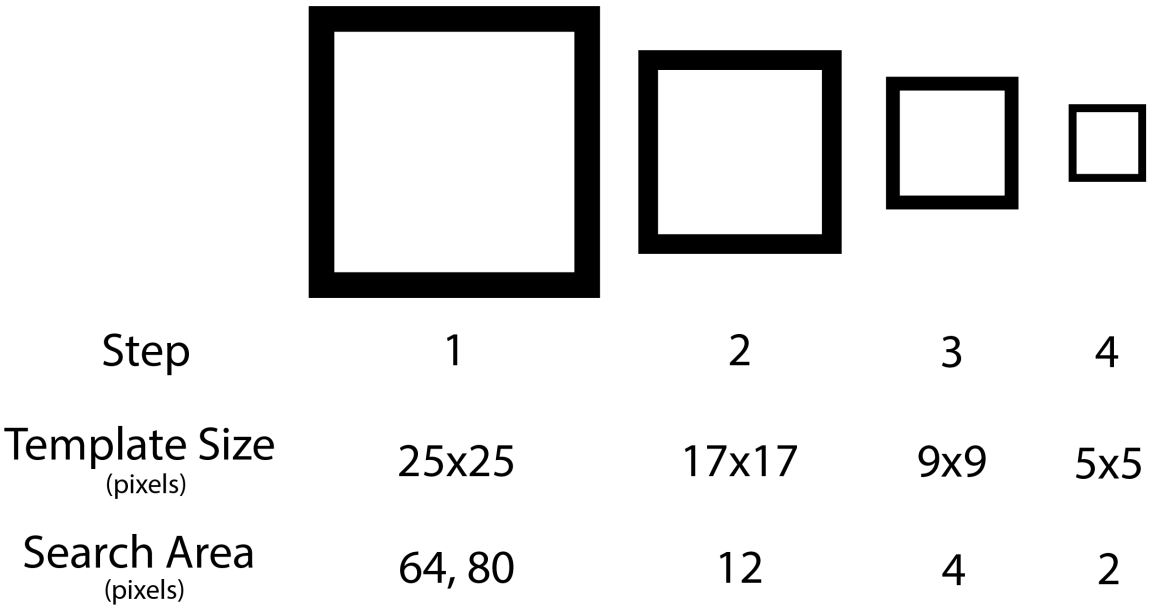

Figure 2.3: Illustration of the Iterative Process. For each iteration the template size and search area are decreased.

After the first iteration, each additional iteration starts with the prior disparity array as a reference and revises each gridpoint's disparity value. The final iteration yields a disparity field capable of resolving both macro and microscale features, as it is the cumulative result of all iterations. As previously stated, the GOES images needed to be rebinned to decrease computational time. The images used in the first iteration are rebinned to be 4 times coarser than native resolution and in the second iteration to be 2 times coarser while the final 2 iterations are at the native resolution. Without this, a process of four iterations and a GOES image of this resolution would take weeks with the computational resources available. Rebinning is necessary to exponentially reduce the computational time required. The resulting disparity array after each iteration also has the same coarsened dimensions of the rebinned GOES image. To rescale

the disparity array to the native dimensions it is "magnified" using bilinear interpolation after each iteration.

4. Quality Control

The resulting disparity array after the first iteration contains a lot of noise and needs to be quality controlled. The first iteration is quality controlled through filtering and smoothing. One of the larger issues the algorithm has is matching at the cloud edge. At the cloud edge there were instances of either large disparity values where there was no cloud, or near zero where there was a cloud. To filter, the IR image from the reference satellite, GOES-16, was compared to the disparity image. Since these images are comparable in space, each infrared pixel value can be compared to the corresponding disparity value. If the infrared value was less than 220 K and the disparity was less than 45 pixels then the disparity value was set to the 95th percentile of all disparity values colocated with an infrared temperature of less than 220 K. The subsequent iterations will determine what the actual disparity value should be by narrowing in on smaller resolution features. This fixes the disparity values near zero where there should be a cloud since colder cloud tops are a good indication of high cloud tops. In addition, if the infrared temperature is above 273 K and the disparity value was above 15 the disparity was set to 10. This fixes the problem where there was no (or shallow, low-level) cloud by allowing later iterations to minimize the value to a more appropriate solution. However, thin cirrus is not measured well by infrared and could fall into this category and be ultimately set to 0 (Lee et al. 2020). Assigning CTHs to thin cirrus is not an objective of this study and is therefore a limitation of the algorithm. These values were decided through extensive, rigorous trial and error to determine which combination of boundaries led to the most stable/reliable performance. After the filtering process the disparity array was smoothed using a median filter of the equivalent

size of the template used for the matching process. Other smoothing methods such as gaussian and boxcar were tested as well but a median smoothing had the best results and was the least aggressive. The disparity fields resulting from the second, third, and fourth iterations are not smoothed or filtered.

After the final iteration each timestep goes through a time filter. Every timestep is compared to the timestep before and after, each at most a 1 minute difference. Only for the purpose of this filter, a 21x21 pixel horizontal median smoother is applied to the neighboring timesteps. At each gridpoint the average of the disparity value of the neighboring timesteps is calculated. This average is then compared to the disparity value of the current timestep and if the difference is greater than 5 pixels the current disparity value is replaced with the average of the neighboring timesteps. This filters out artifacts generated from the matching process that cannot be filtered out using IR or the spatial median filter outlined above. An example of a supercell from 22 May 2020 at 2340 UTC is shown in Figure. 2.4. Areas of poor matching for this timestep, most noticeably at the cloud edge, were replaced with a more realistic solution.

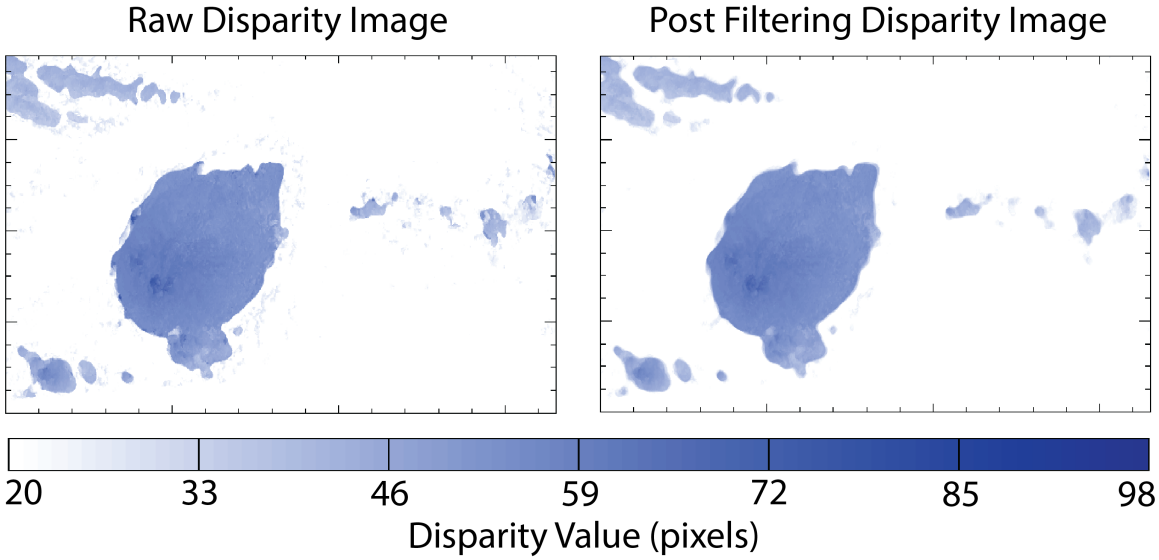

Figure 2.4: Raw disparity values (left) and filtered disparity values (right) after 4 iterations are shaded in blue from 22 May 2020 valid at 2340 UTC.

Additional testing of not only smoothing the disparity array, but also smoothing the GOES images being fed into the stereoscopy algorithm was also explored. Multiple combinations of smoothing techniques, including spectral filtering, and smoothing dimensions were examined. It was determined smoothing the GOES images was not beneficial to the performance of matching GOES images.

5. Calculate CTH

   Once the final iteration of disparity values is populated and time-filtered the disparity values have to be converted to CTH for analysis. There are several methods to achieve this with two of the most common being trigonometric and iterative approaches. The trigonometric method uses the calculated distance of the parallax, satellite zenith angle, and azimuth angle to geometrically calculate the CTH. The iterative method uses assumed CTH to calculate the parallax which is then compared to the disparity value calculated in the previous step to find the minimum difference between the two. The iterative approach was adopted in this case because it allows a choice in the vertical resolution of CTH calculated and therefore the CTH quality can be evaluated at each gridpoint. After comparing results using both methods Lee et al. (2020) found the accuracy to be similar with a correlation coefficient of 0.99.

   To calculate the parallax at various cloud top heights, several geometric variables need to be calculated at each height to obtain the longitude the cloud is projected to for each satellite. An illustration to better understand these geometric relationships can be found in Sandmæl (2017). With the longitudes the longitudinal difference between each satellite's projection can be calculated and related to disparity values. First, the central angle between the satellite and the cloud location (α_{c_c}) is calculated using Equation 2.2.

$$\alpha_{c_c} = 2 \cdot arcsin\sqrt{(sin\frac{y_s - y_c}{2})^2 + cosy_s \cdot cosy_c \cdot (sin\frac{x_s - x_c}{2})^2} \tag{2.2}$$

Where y_s is the latitude of the satellite, y_c is the latitude of the actual cloud position, x_s is the longitude of the satellite, and x_c is the longitude of the actual cloud position. The central angle is then used to find the distance between the satellite and the cloud top (d) using the Law of Cosines.

$$d = \sqrt{h_s^2 + h_{c_t}^2 - 2 \cdot h_s \cdot h_{c_t}^2 \cdot s\alpha_{c_c}} \tag{2.3}$$

Where h_s is the height of the satellite and h_{c_t} is the height of the cloud top. With this distance the satellite viewing angle (α_{s_v}), the angle between the center of the earth and the cloud top height, can be computed.

$$\alpha_{s_v} = arccos\frac{h_s^2 + d^2 - h_{ct}^2}{2 \cdot h_s \cdot d} \tag{2.4}$$

The satellite viewing angle is used to find the viewing angle at the projected cloud point between the satellite and center of the earth (α_p) using the Law of Sines. This angle is then used to find the angle between the projected cloud point and the satellite (α_c).

$$\alpha_p = arcsin\frac{h_s \cdot sin\alpha_{s_v}}{r_E} \tag{2.5}$$

$$\alpha_c = \pi - \alpha_p - \alpha_{s_v} \tag{2.6}$$

Where r_E is the radius of the Earth. To find the latitude of the projected cloud point (y_p) latitude replaces the angles in equations (α_{s_v} through α_c). Finally, Equation 2.7 is used to compute the longitude at which the cloud top is projected to (x_p). The sign of the second term is dependent on whether the cloud is to the east or west of the longitude of the satellite.

$$x_p = x_s \pm 2 \cdot arcsin\sqrt{\frac{(sin\frac{\alpha_c}{2})^2 - (sin\frac{y_s - y_p}{2})^2}{cosy_s \cdot cosy_p}} \tag{2.7}$$

As previously stated, only the longitudinal parallax is significant and only the difference in x_p calculated between both satellites at varying cloud top heights needs to be considered. To be comparable, the disparity values calculated in the previous step are converted to degrees. At each gridpoint the parallax was calculated for CTH's increasing in increments of 200 meters. At each gridpoint the parallax retrieved from the previous step is then compared to each theoretical CTH parallax. The height with the smallest difference is assigned as the CTH for that gridpoint. Lastly, since the parallax correction was done in reference to the GOES-16 image, the CTH image needs to be parallax corrected to be in the position of the actual cloud, which is a simple backwards matching operation when using the iterative method. The image was parallax corrected from the GOES-16 position based on retrieved cloud top heights. This parallax correction method relies on accurate CTH retrievals to correctly place cloud features.

Chapter 3

Results and Discussion

3.1 Case Studies

This section will review 6 cases where overlapping GOES imagery was analyzed by the stereoscopic CTH retrieval algorithm developed for this study. Table 3.1 breaks down the location and time period for each case. These cases include varying mesoscale phenomena from discrete supercells to mesoscale convective systems (MCSs). It was important to include a variety of convective modes to analyze how the algorithm performs with different types of cloud fields. Figure 3.1 overlays the selected storm starting locations on a map of GridRad's vertical sampling (assuming all radars are operating in convective mode).

Case Studies 2019-2021				
Case Date	**Central Lat/Lon (GOES-16)**	**Time Period (UTC)**	**1st Iteration Search Area (pixels)**	**Number of Storms Tracked (subsection)**
5/17 - 5/18/2019	41.898 N, 100.259 W	23:30 - 02:00	64	6
5/13 - 5/14/2020	34.512 N, 100.375 W	19:30 - 01:00	64	74
5/22 - 5/23/2020	33.888 N, 97.083 W	22:30 - 01:00	80	22
6/8 - 6/9/2020	44.146 N, 98.396 W	22:30 - 01:30	80	19
4/6 - 4/7/2021	38.979 N, 97.039 W	22:30 - 00:30	80	11
4/23 - 4/24/2021	32.450 N, 97.133 W	21:30 - 00:30	64	40

Table 3.1: Table describing all cases included in this study. Cases which were requested through the Satellite Analysis Branch are bolded.

For each case a sub-domain of the full overlapping domain will be presented to focus on the area of deepest convection. Data quality and performance of the stereo algorithm will be examined through a comparison of stereo retrieved CTH and echo top heights. For each case a history map of 20 dBZ echo top altitudes, maximum

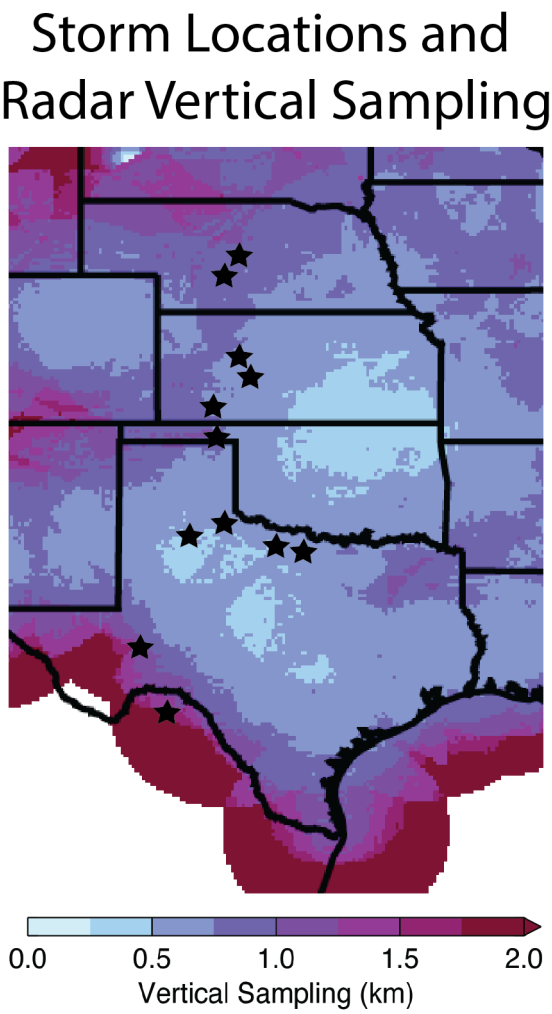

Figure 3.1: Selected storm track origins (stars) and NEXRAD WSR-88D vertical sampling in VCP-11 mode of the 0-20 km ASL altitude layer.

stereo altitudes, tropopause relative heights for both data sets, reflectivity, and IR from GOES-16 is composed. Cases will be presented from oldest to most recent.

Storm reports used to describe the storm timeline and severity were retrieved from the Severe Prediction Center (SPC) archive. Significant hail reports, which SPC defines as >2 in, will be included in the analysis if they exist. The height of 20 dBZ reflectivity echo tops was determined using GridRad data. The 20 dBZ threshold was enforced because at higher altitudes lower dBZ data points are more likely to be unreliable due to radar artifacts. For data quality purposes, for a level to

be considered an echo top, the two layers below were also required to be higher than 20 dBZ. For the purpose of comparison, all history maps shown for each case have data plotted only where these echo tops were observed.

On 17 May 2019, a couple of discrete supercells developed near the Oklahoma and Kansas border minutes before 0000 UTC. Both storms tracked NNE and continued to progress after sunset. Both storms formed OTs shortly after initiation while the southern storm also produced significant hail and a tornado. The tornado was reported as a large wedge tornado later in its lifetime after 0230 UTC, later rated an EF3 on the Enhanced Fujita scale. Both storms stayed discrete through the end of the stereo analysis period (close to sunset).

Figure 3.2 is composed of the maps described above. The stereo algorithm was not run over the northern half of the northern storm because overlapping GOES imagery did not exist for that region. This can be seen in Figure 3.2 subplot B and D where the northern edge of the GOES-17 domain restricts any possibility of stereo analysis. Figure 3.3 shows 20 dBZ echo tops reached up to 17 km for storm Track 2, the northmost storm, which was 4 km above the tropopause. When compared to the retrieved CTH from stereo, the highest stereo heights were about 15.5 km at the same time, failing to reach the heights seen from echo tops. The stereo algorithm underestimated the echo top heights in overshooting regions and the assumption of underestimating actual CTH can also be made. This underestimation from the stereo retrievals occurred often within the OT region in many of the cases that will be presented below.

A slight offset in the swath of highest CTH and the swath of highest echo tops can be seen from the tropopause relative maps in Figure 3.2. This displacement can have three possible explanations. First, the echo tops and cloud features like OTs do not align perfectly with each other. This can be from wind advecting hydrometeors downstream from the updraft which creates a separation of the cloud features being

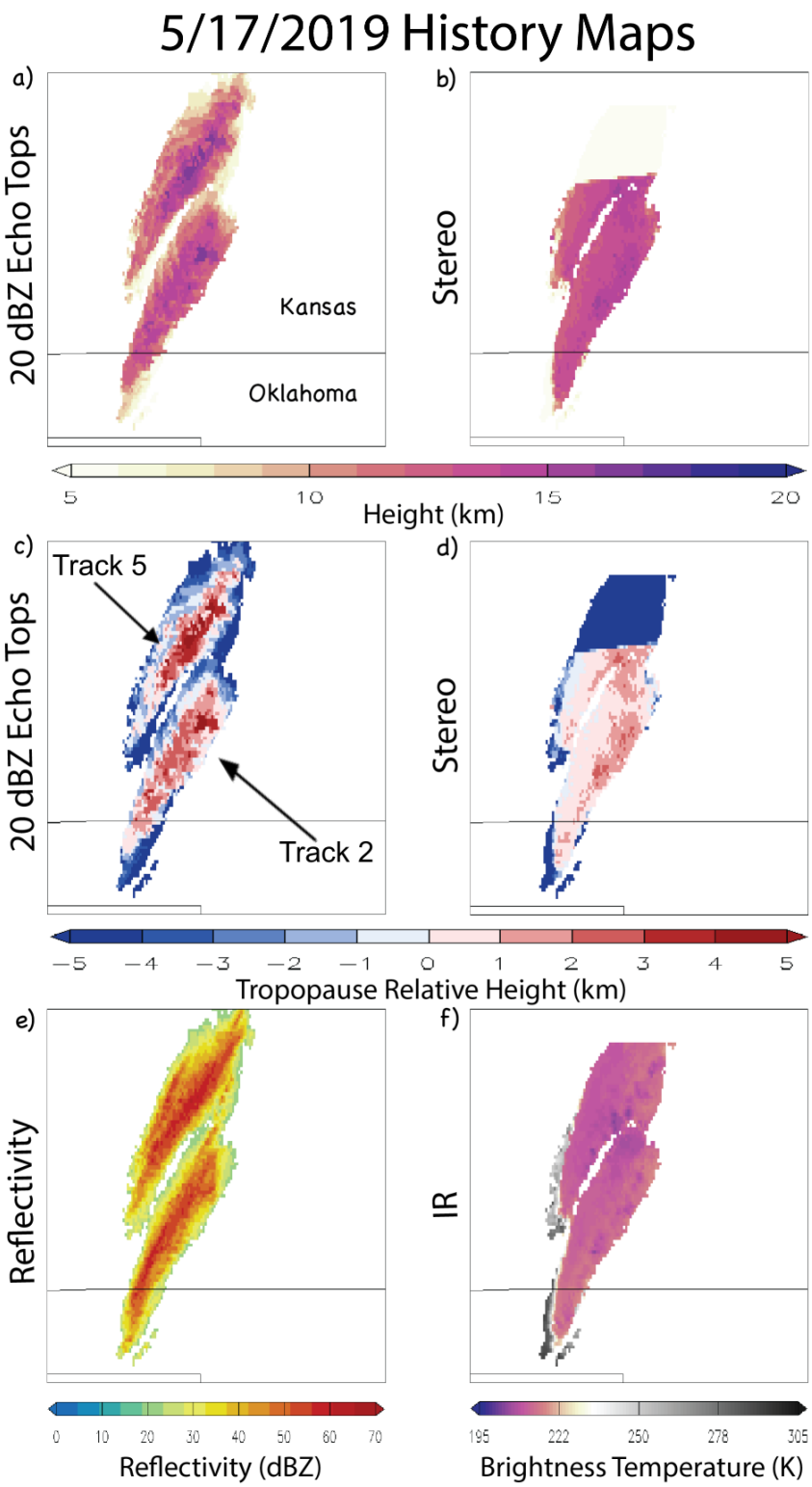

Figure 3.2: History maps from 17 May 2019 of a.) maximum 20 dBZ echo top height b.) maximum stereo c.) 20 dBZ echo top tropopause relative height d.) stereo tropopause relative height e) maximum reflectivity f) minimum IR temperature.

matched through stereo and the hydrometeors detected by radar. Second, in the final step of the stereo algorithm, when calculating CTHs, assumes the shape of the Earth as an ellipsoid. Since the Earth is not a perfect ellipsoid, this assumption creates localized regions that deviate from the ellipsoid on the order of tens of meters (Fujita, 1982). This error is relatively small when compared to the CTHs being calculated. Lastly, the stereo retrieval fails to retrieve fine scale OT features which leads to an underestimation of CTHs. This underestimation does not allow for a full parallax correction to be performed in regards to the placement of fine scale cloud features.

To better resolve and analyze individual storms, the storm tracking method used in Homeyer et al. (2017) and Sandmæl et al. (2019) was applied to the GridRad data sets. This method outputs individual storm tracks via an echo top algorithm. Specifically, at each 5-minute interval in GridRad data, local maxima of 40 dBZ echo tops are linked in time if they reside in close proximity to each other. These storm tracks are then linearly interpolated to account for the highest temporal resolution data set, stereo retrievals, being at 1-minute resolution. Since GridRad data is available at 5-min intervals it is linearly interpolated to 1-min intervals to account for the highest temporal resolution data available. Since this assumes a continuous storm motion, errors can result from a non-uniform storm motion in each 5-min period.

Two storm tracks, Track 5 from the main updraft of the northern storm and Track 2 from the main updraft of the southern storm were manually selected for analysis. For a more in depth comparison, Figure 3.3 shows stereo CTH and echo top heights for the lifetime of both storms. The blue dotted lines encompasses the up to ± 1 km possible error for the echo top heights in most regions. The tropopause taken from MERRA-2 reanalysis data generally has a high bias and is accurate to within 0.5 km (Xian and Homeyer, 2019). Both storms were penetrating the tropopause the entirety of the time the storm track algorithm detected them, most of the time by several kilometers. Echo tops and stereo CTH generally stay close to each other in

Track 2 but stay towards the bottom end of the echo top envelope for most of Track 5. CTH retrievals having a slight bias to the bottom half of the echo top envelope is a common theme for most overshooting storms. According to SPC, based on radar and reports the best estimate for initial formation of a tornado for the southern storm (Track 2) was 0035 UTC. The stereo analysis of Track 2 in Figure 3.3 shows a rapid increase in CTH in the 5 minutes before tornado formation.

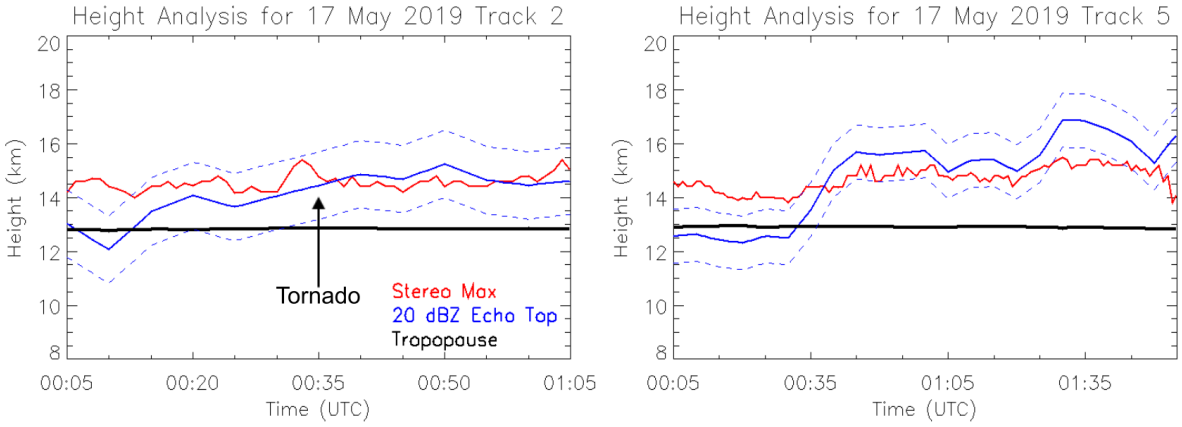

Figure 3.3: Time series analysis of stereo height (red), 20 dBZ echo top height (blue) and error (dashed blue), and tropopause height (black) of storm tracks 2 and 5 from 17 May 2019, identified by the storm tracking algorithm. Error bars are 1.25 km and 1 km for Track 2 and 5, respectively. These error bars are extracted from the 0-20 km average vertical sampling from GridRad shown in Figure 3.1.

In contrast to the previous case, two separate lines of storms and colliding supercells existed on 13 May 2020. Around 2000 UTC storms started forming in western Texas and south of the Texas and Mexico border. One storm became dominant in west Texas while an MCS formed to the north in the Texas panhandle and progressed east. The MCS had several hail reports while the southern storms lacked any reports. The southern storms traveled through unpopulated areas, reducing the liklihood of severe reports associated with the track..

The three distinctive regions of storms which will be discussed are the MCS in north Texas, the dominant supercell in west Texas, and the storm south of the Texas border in Mexico. All three storms were overshooting the tropopause for the majority

of their lifetimes. Starting with Track 18 which is the storm in Mexico, shown in Figure 3.5, the echo tops reach over 18 km while stereo retrievals indicate maximum CTHs of about 16 km. This region has very poor radar coverage since the closest and only radar to sample it is in Laughlin AFB, Texas (KDFX). The vertical sampling at high altitudes in this region is greater than 2 km as shown in Figure 3.1. Unlike the up to 1 km error assumed on the analyses plots, the error for echo tops in this region is likely greater than 2 km. This is an example of stereo analysis being the superior indicator of true CTHs in an area of poor radar coverage. Track 30 was associated with a storm cell within the MCS in north Texas. Heights taken from echo tops and stereo were in good agreement until the end of the storm track time period. At this time the cell was weakening and larger hydrometeors were not being lofted as high because of a weakening updraft. However, the CTHs stayed relatively constant because echo tops fall far in advance to the actual cloud tops. Echo tops are more reflective of the weakening trend than CTH because the cloud field will still exist well past storm dissipation.

Track 69, the storm in west Texas, recorded the highest echo tops for this case. Most noticeable in the height analysis plot is the spike in stereo CTH 10 minutes before the rapid increase in echo top heights at 2240 UTC. After this initial spike both heights track each other well for the rest of the analysis period. It is expected for CTH increases to precede echo top increases. This time lag is because lofting hydrometeors higher in altitude is slower than lofting cloud material.

Unlike Track 5 from the previous case, the stereo algorithm did retrieve similar CTH heights compared to echo top heights for overshooting storms. The placement and height of the overshooting regions is also comparable between echo tops and stereo. CTH from stereo analysis also depicts the extent of the anvil cirrus which radar does not. The CTHs drop off quickly to the east of the storms in the echo top maps while the CTHs stay fairly constant to the east in the stereo maps. This

is due to the upper most portions of the cloud advecting east because of the upper level winds. Clouds are advected downwind and stay at constant to slight decreasing heights while precipitation does not advect far downstream and quickly falls to the ground.

The highest OTs analyzed with the stereoscopic algorithm were from 22 May 2020. A right moving supercell tracked along the Red River to the ESE with its storm motion deviating from surrounding storms. At 2330 UTC another storm initiated to the southeast which would eventually collide and merge with the dominant right-mover after 0100 UTC. The storm moving along the Red River is labeled as Track 14 while the storm that initiated at 2330 UTC to the SE is labeled as Track 12. Both storms produced tornadoes and significant hail. The first report of a tornado from the storm moving along the Red River was at 2311 UTC and the first report of a tornado from the storm to the SE was at 0023 UTC.

Comparable to the previous case, a larger area of CTHs above the tropopause compared to echo tops can be seen in Figure 3.6. This will be apparent in every case. Looking closer, a comparison of echo top to stereo CTHs from Track 12 are very close throughout. Similar to storm tracks from the 17 May 2019 case, the CTHs are underestimated and stay close to the bottom of the echo top error envelope for Track 14. Echo top heights from Track 14 imply CTHs above 18 km which is about 5 km above the tropopause. Considering these echo top heights, the stereo algorithm struggled to capture the extent of the overshooting for most of the storms lifetime. This underestimation is later discussed in Section 3.2.

On 8 June 2020, a cluster of storms developed across Central Nebraska. The first storms initiated just prior to 2300 UTC and moved to the NE, staying discrete and never growing upscale into a continuous line of storms. A tornado was first reported from the southernmost cell at 2350 UTC. In addition, up to tennis ball sized hail was reported from the same storm at 0115 UTC.

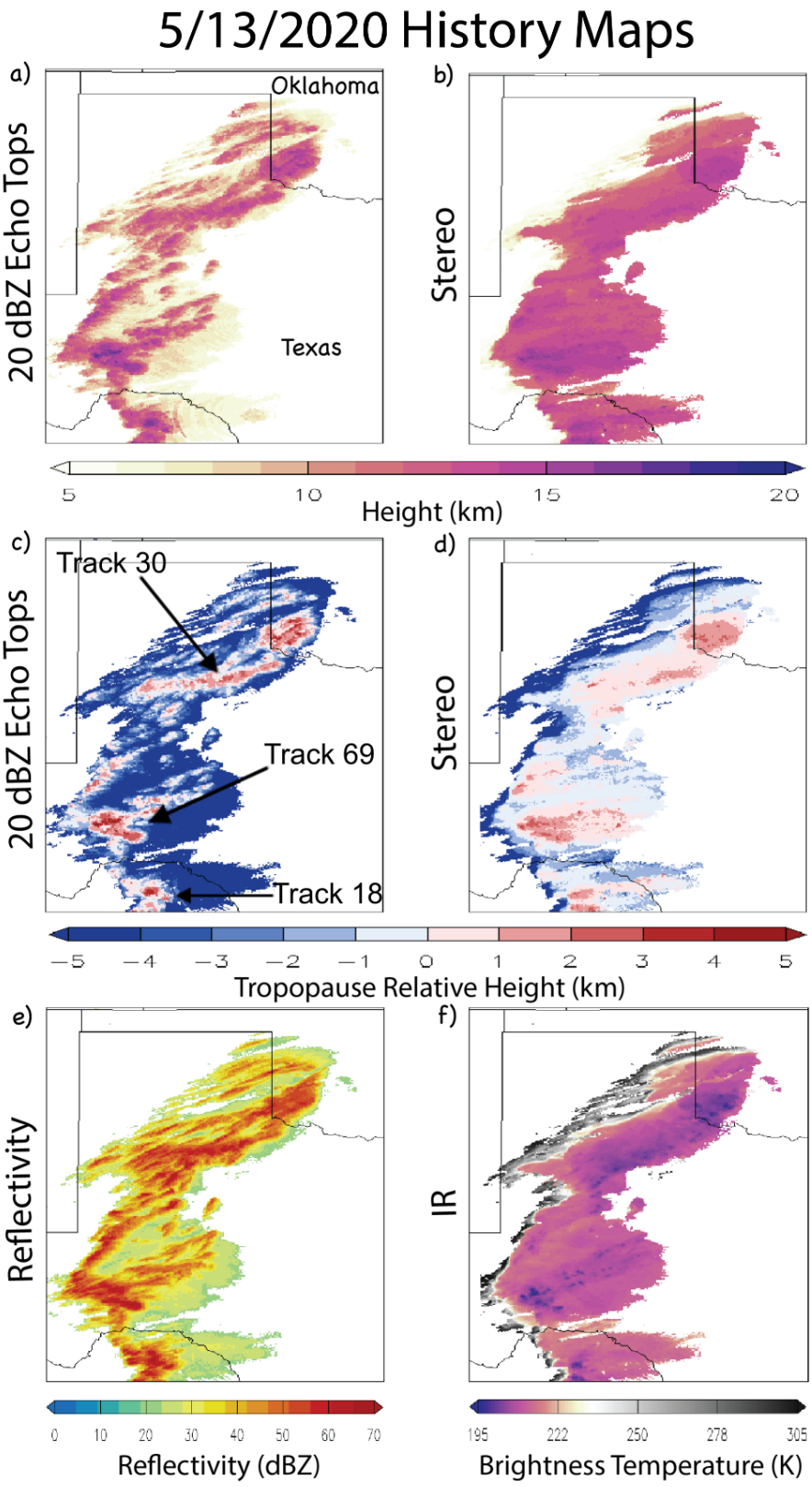

Figure 3.4: As in Fig. 3.2, but for 13 May 2020.

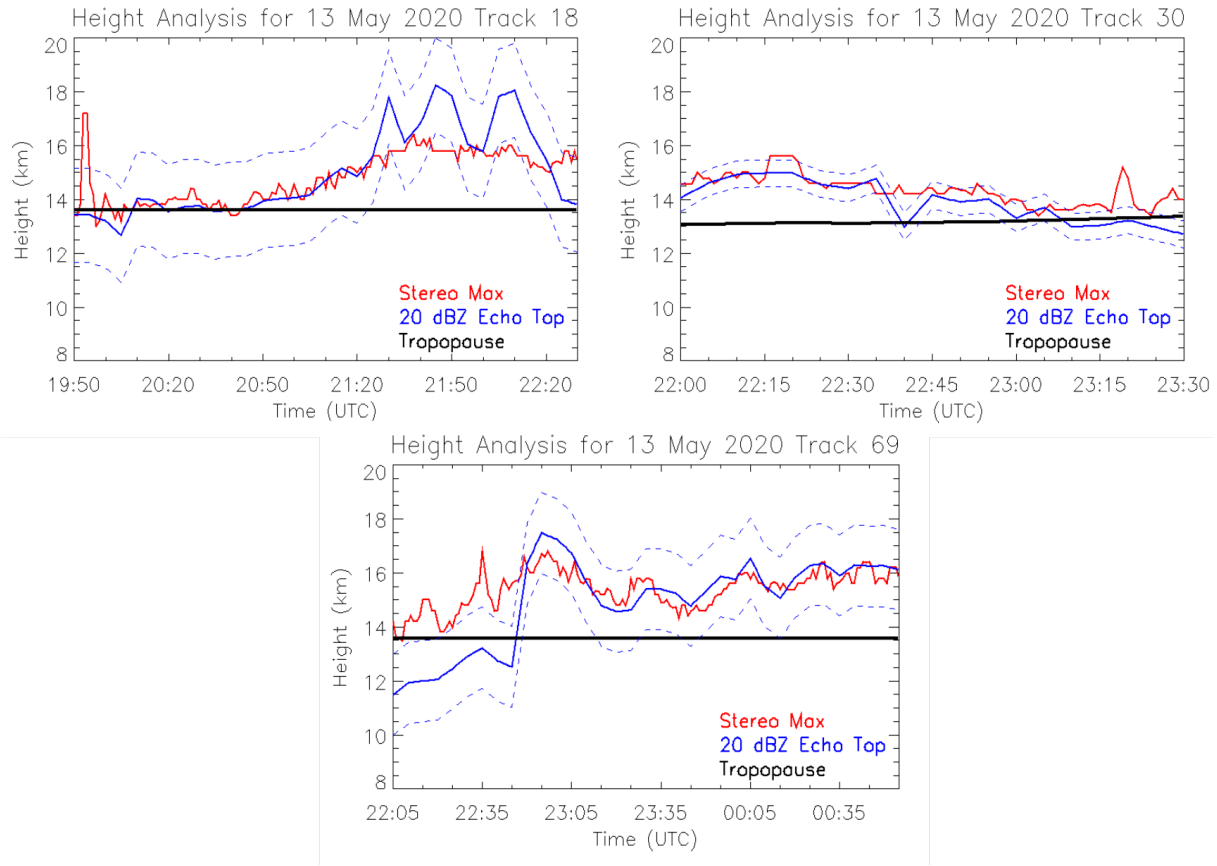

Figure 3.5: As in Fig. 3.3, but for tracks 18, 30 and 69 from 13 May 2020. Error bars are 1.75 km, 0.5 km, and 1.5 km, respectively.

Similar to the storm south of the Texas border on 13 May 2020, the radar coverage in Central Nebraska is poor. The average vertical sampling up to 20 km ASL in GridRad is higher than the assumed error of 1 km. The history maps shown in Figure 3.6 paint a similar picture to previous cases of the inability for stereo CTHs to capture the highest OTs. The stereo CTHs from Track 13 (tornadic southern cell) and Track 15 (immediately to the north of Track 13) do not resolve the pulses of increasing echo top heights. The CTHs stayed relatively constant just above the tropopause for both storms.

The next two cases, 6 April 2021 and 23 April 2021, are early spring severe events with lower tropopauses compared to the mid to late spring events described above. The first echoes were detected in central Kansas on 6 April 2021 just before 2200 UTC.

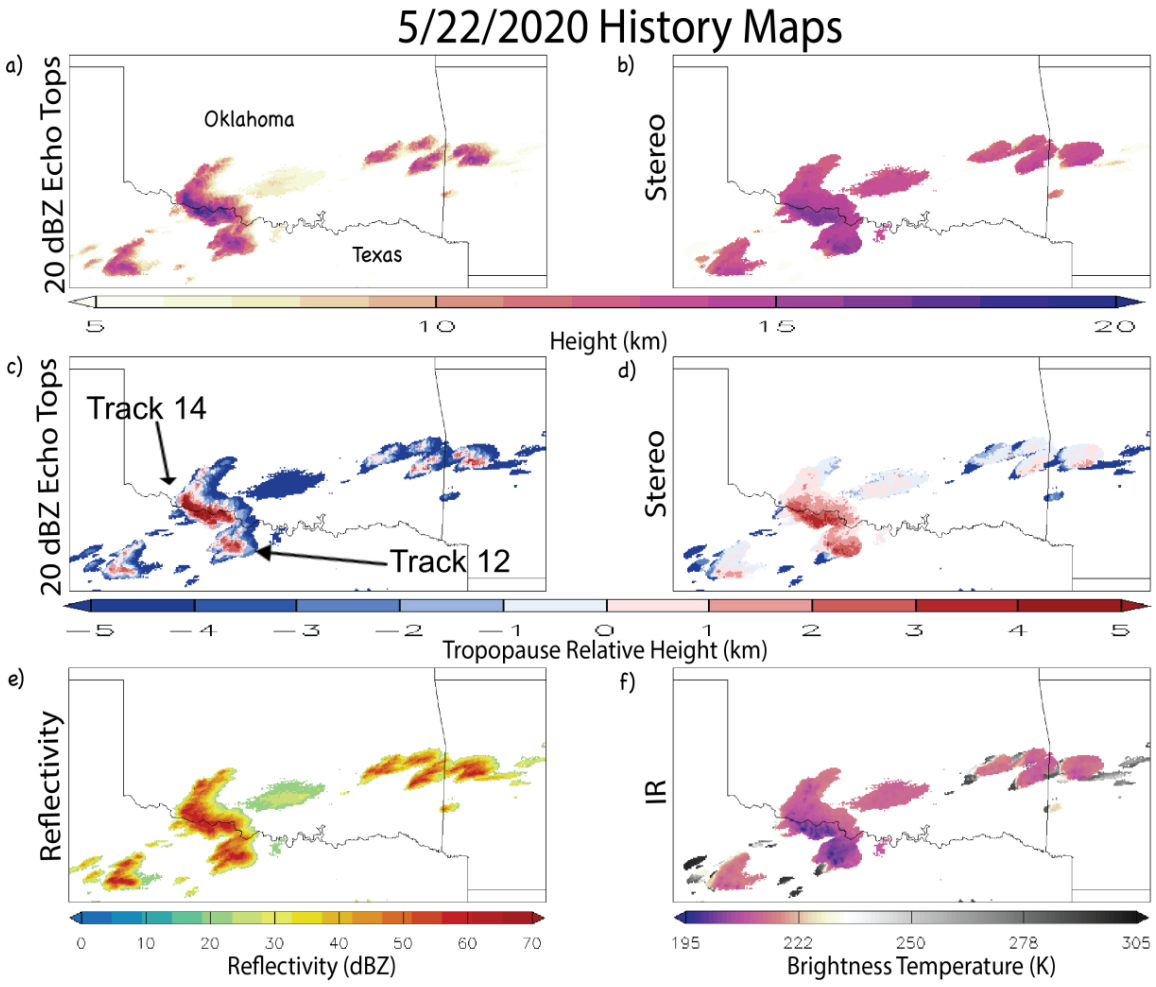

Figure 3.6: As in Fig. 3.2, but for 22 May 2020.

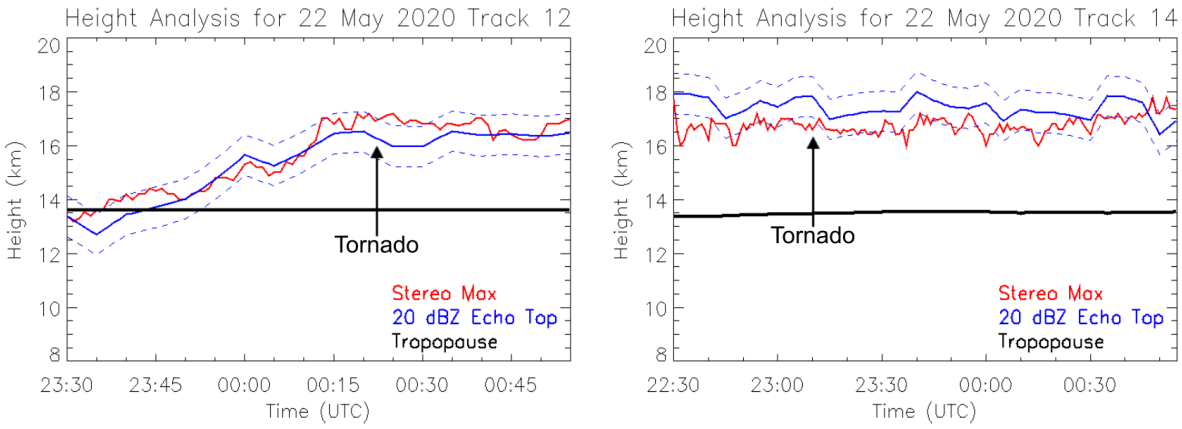

Figure 3.7: As in Fig. 3.3, but for tracks 12 and 14 from 22 May 2020. Error bars are 0.75 km for both tracks.

Several storms developed and grew upscale into an MCS after 0200 UTC. There was a report of significant hail from the southernmost cell at 2345 UTC.

There are two separate regions of convection illustrated by GridRad data shown in Figure 3.10. One region, which will be the area of focus for this case, encompasses the storms in central Kansas, the other region encompasses the storms that initiated in southern Nebraska. The storms that initiated in Nebraska were not covered by stereo analysis because of a lack of overlapping GOES data. An initial review of the tropopause relative maps shows several isolated areas of echo tops heights about 1 km higher than the highest CTHs retrieved from stereo. This reiterates the trend of the stereo analyses falling below echo top consensus in regions of deepest overshooting. Both Track 7 and Track 9 generally follow the echo top evolution closely, with Track 9 even favoring the higher end of the error envelope. Track 7 corresponds with the most southern storm cell and Track 9 corresponds with the very close neighboring storm cell directly to the north.

On 23 April 2021, a dominant supercell track south of the Red River for several hours. The supercell became tornadic shortly after 2230 UTC. As this storm moved to the southwest, several smaller cells collided and merged with this larger supercell after 2330 UTC. The last report of a tornado being produced was at 2342 UTC.

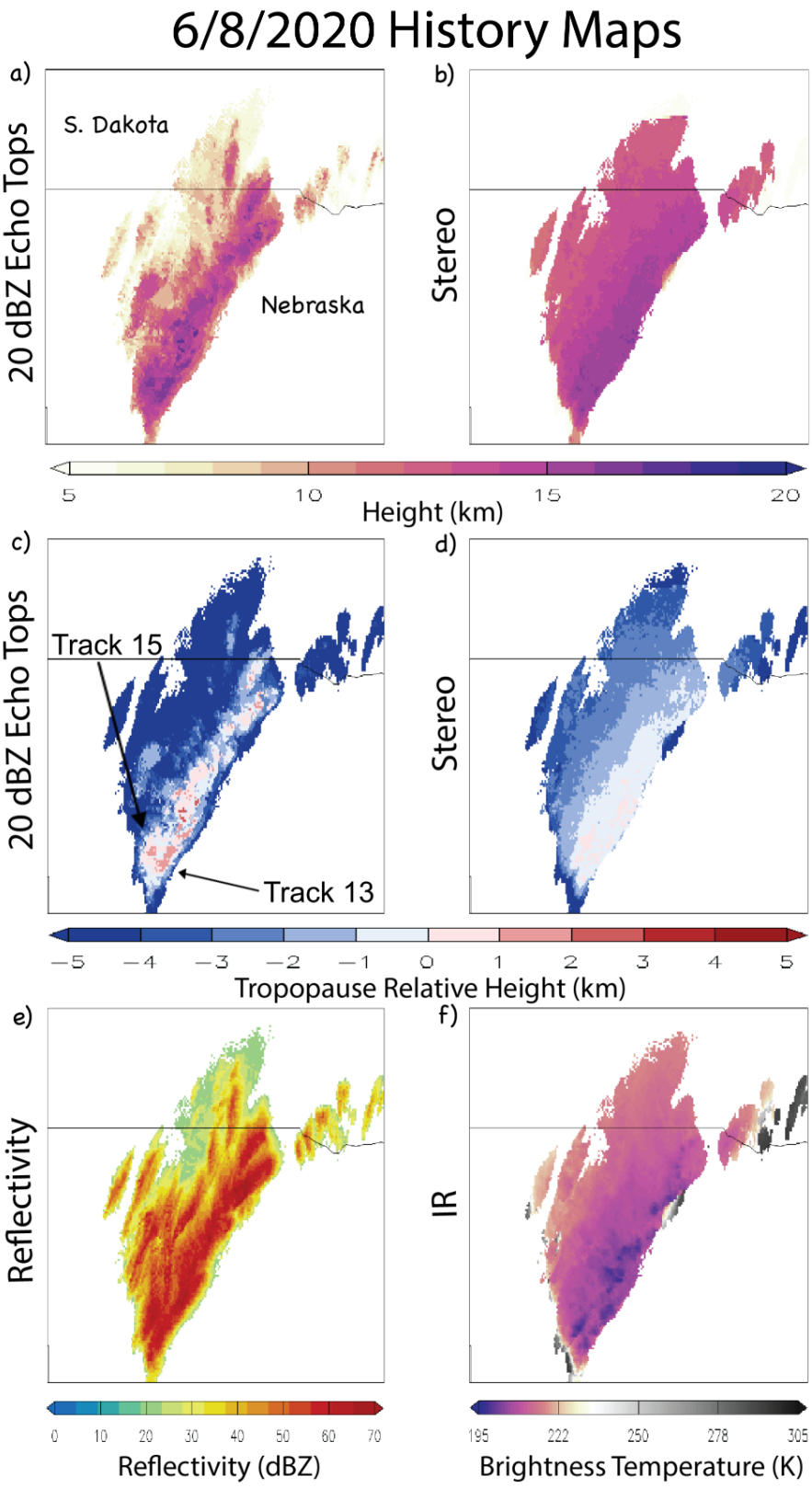

Figure 3.8: As in Fig. 3.2, but for 8 June 2020

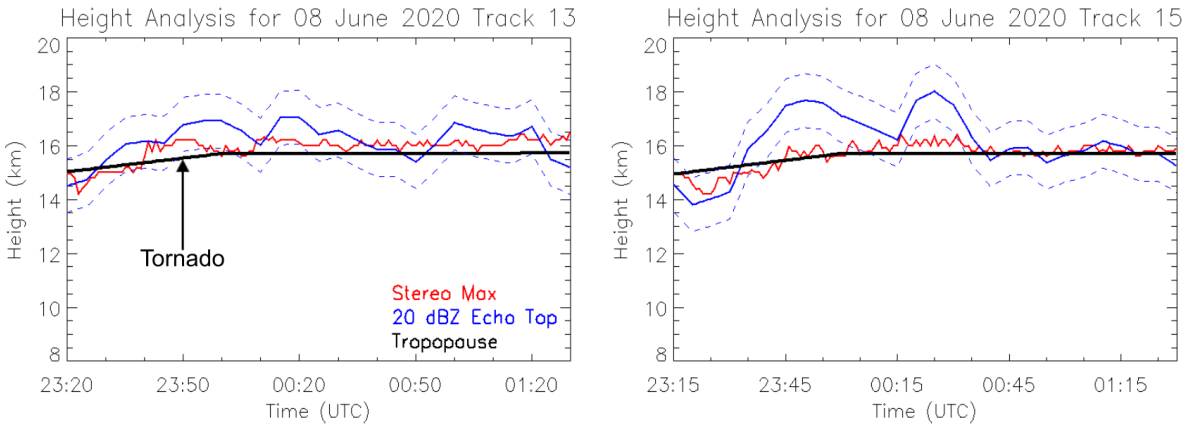

Figure 3.9: As in Fig. 3.3, but for tracks 13 and 15 from 8 June 2020. Error bars are 1 km for both tracks.

In addition to producing several tornadoes, the storm was responsible for producing significant hail up to 2 inches in diameter.

Similar to the previous case the tropopause-relative height maps depict the maximum stereo CTHs lower along the track of the dominant right moving supercell. The time analysis of this supercell, labeled as Track 34, further shows the time evolution of the stereo heights tracking along the lower edge of the error envelope for the echo top heights. Of note is the spike and quick fall in CTHs at 2205 UTC, approximately 30 minutes before the first tornado report.

3.2 Limitations of Stereoscopy Algorithm

Specific examples from storm tracks in the previous section show the stereoscopic retrieval algorithm has its limitations and uncertainties. First, the displacement of the highest heights in the stereo CTH compared to the echo top heights indicates a difference in where the stereo algorithm is placing storms from radar. This can possibly be explained by upper level winds displacing higher cloud material from the updrafts, or an inevitable error when converting the disparity field to CTHs by assuming the Earth is an ellipsoid. By assuming the Earth is an ellipsoid it creates

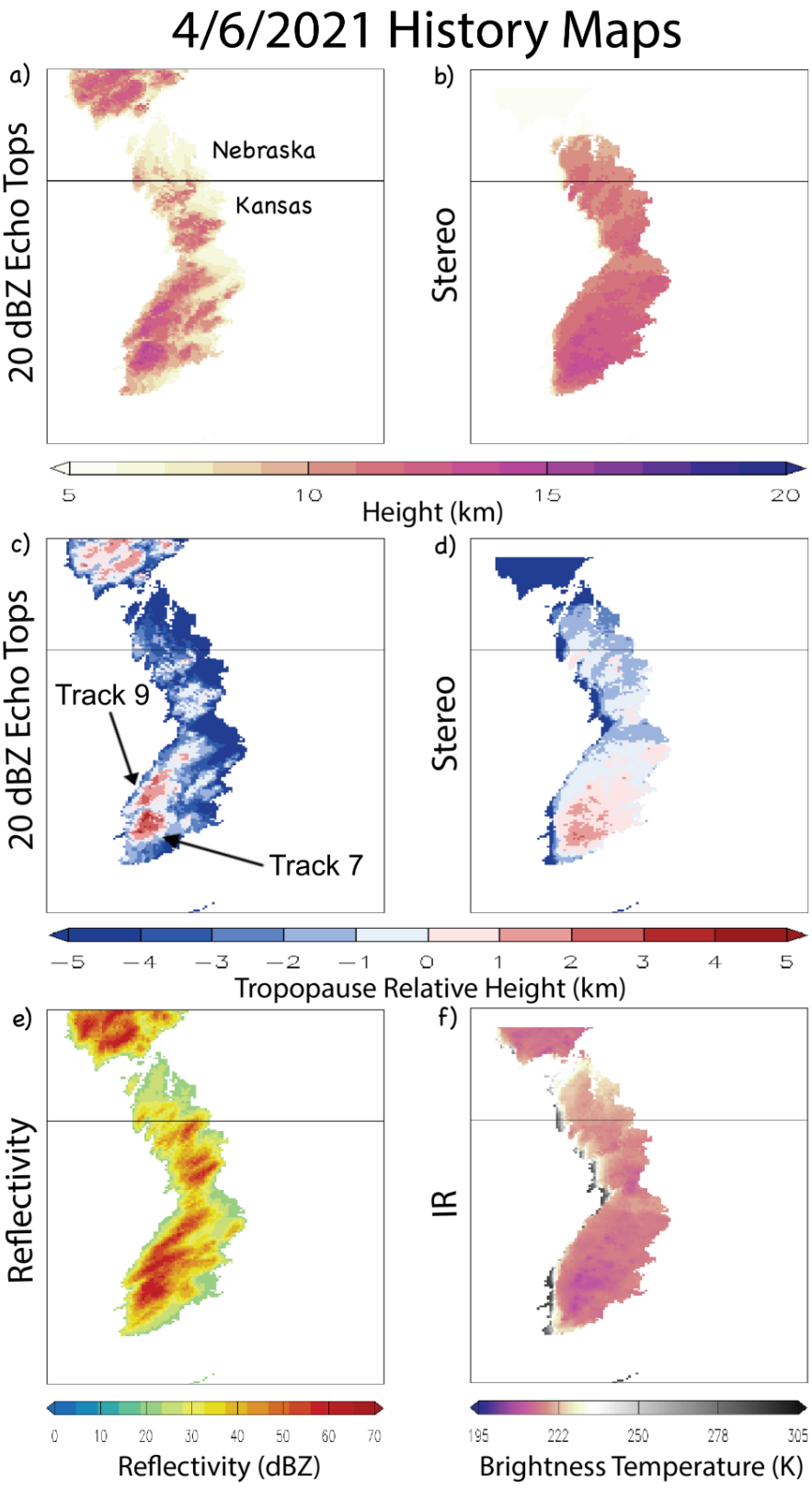

Figure 3.10: As in Fig. 3.2, but for 6 April 2021.

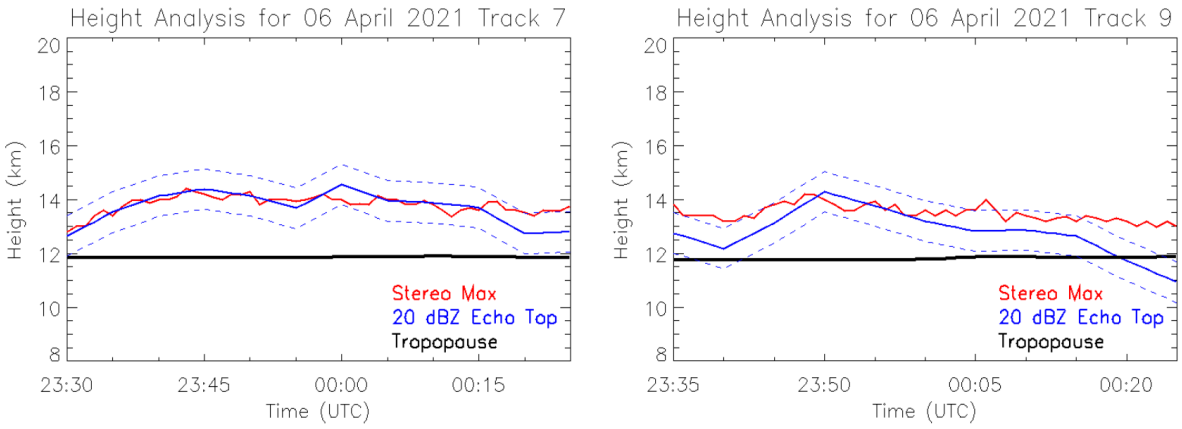

Figure 3.11: As in Fig. 3.3, but for tracks 7 and 9 from 6 April 2021. Error bars are 0.75 km for both tracks.

localized regions of error as discussed in Fujita (1982). As examined previously, underestimation of CTHs in the highest regions will also prevent the parallax from being totally corrected and therefore misplacing them slightly. Second, the actual values being retrieved from stereo are on average underestimating the 20 dBZ echo tops. Figure 3.14 shows an aggregate of all 12 storm tracks selected for a closer analysis in the previous section. 10 dBZ and 20 dBZ Echo tops were subtracted from stereo CTHs meaning negative values represent instances when stereo CTH was lower than the echo tops. The stereo retrieved heights were on average 0.575 km lower than the 10 dBZ echo top heights and 0.104 km lower than the 20 dBZ echo top heights. Although the stereo algorithm is underestimating CTHs this could mean the separation from echo tops to cloud top is smaller than originally anticipated in OT regions. Since it is unlikely radar is vastly overdoing echo top heights at this altitude because of viewing angles, the underestimation by stereo retrievals in regions of overshooting can perhaps be explained by several other hypotheses. It is unlikely radar is overdoing echo tops because these regions are being sampled by multiple radars leading to a higher confidence in an accurate measurement. Next steps of this study can include comparisons to other stereo studies and CTH algorithms such as the GOES ABI CTH product.

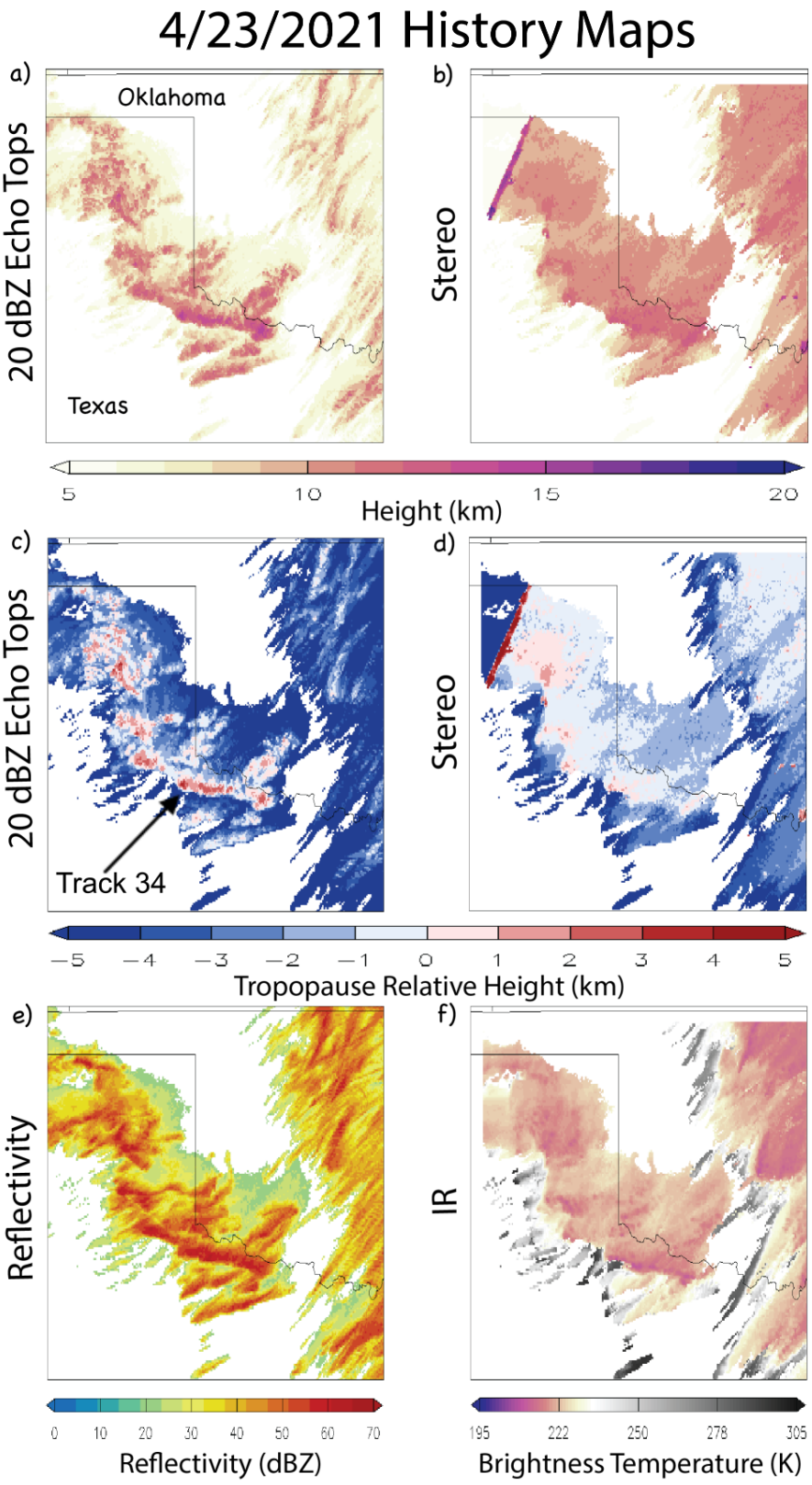

Figure 3.12: As in Fig. 3.2, but for 23 April 2021.

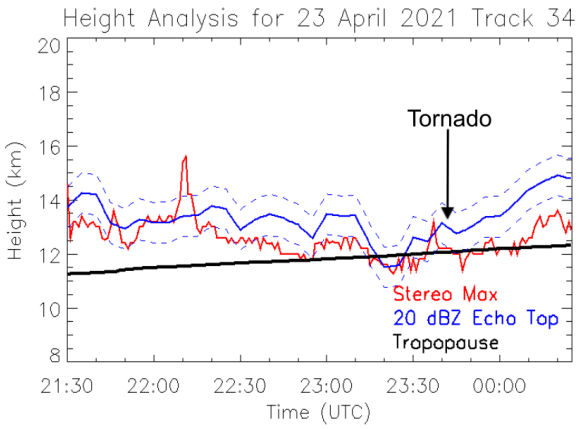

Figure 3.13: As in Fig. 3.3, but for track 34 from 23 April 2021. Error bar is 0.5 km.

It is unlikely the sizing of the templates used in the iterative process would not be able to resolve smaller cloud features since prior studies have demonstrated they can. The finest iteration uses a ∼2 km x ∼2 km template which is small enough to resolve finer cloud features including OTs. Although this combination of template sizes and search areas was found to produce the best results for the storm as a whole, the search area for the first iteration could fail to set up later iterations to converge on an agreed disparity value that would exceed the first iteration's search area. The use of rebinned images in the first and second iterations coarsens the image which does not help in improving match scores for fine scale features such as OTs. While increasing the initial search area would solve this underestimation problem, it would create larger errors elsewhere, most noticeably at the cloud edge. Larger errors in other parts of the storm would require a harsher filter which would harm the ability to resolve finer features. The filters in place could also be preventing OTs from reaching their true height. The filtering in the disparity calculation step as well as the filtering before converting to CTHs could contribute to this. However, further analysis of the grid points that were changed in the latter filter were not concentrated in areas of overshooting. This would eliminate the latter filter from being the source of this error. Alternatively, a hybrid approach, utilizing strictly IR imagery in the final iterations,

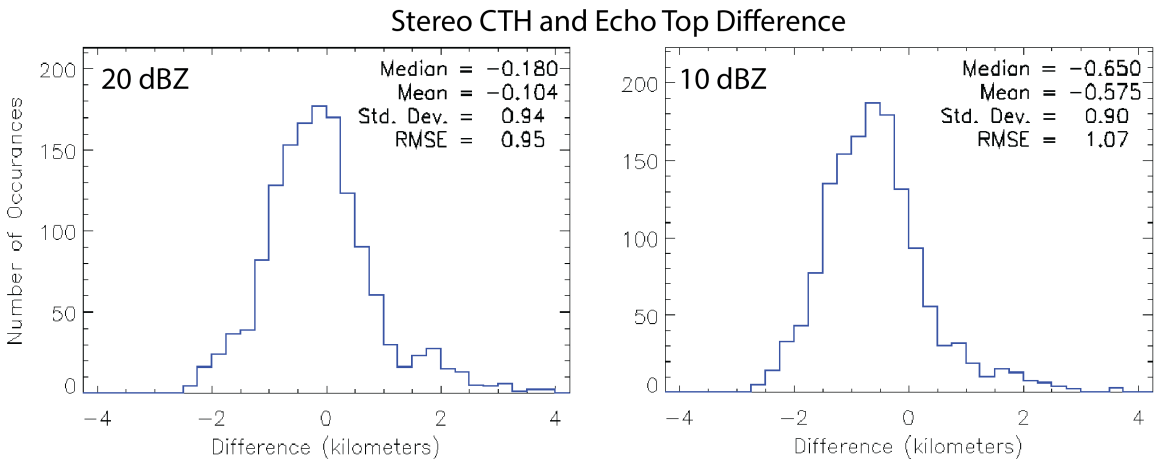

Figure 3.14: Aggregate of the difference in stereo heights and 20 dBZ echo top heights (left) and 10 dBZ echo top heights (right) from storm tracks presented in this study.

could help resolve the highest CTHs. For example, the final two iterations could use IR imagery instead of visible, which would negate the light reflectance issue, and help resolve the highest CTHs. Unfortunately, this alternative approach would resort to coarser imagery compared to visible imagery.

In the algorithm itself, steep cloud slopes and the storm's anvil or high cirrus masking the core of the storm could be inhibiting the matching process from finding strong matches. Because of the large degree of separation between GOES-16 and GOES-17, steep sloping overshoots can block parts of the storm from view. The steep slopes are also illuminated differently from different points of view contributing to a complete difference in appearance from each satellite. Figure 3.15 shows a 80x80 pixel area of the same overshoot from the 22 May 2020 supercell. Without prior knowledge of these images, it would be difficult for someone to match these images to the same location and time. Additionally, high level cirrus and anvil masking the core of the storm create an additional barrier to successful matching. As also found in Lee et al. (2020), comparing clouds with little texture and therefore barely any uniqueness, such as cirrus, is very difficult to produce reliable matches. This cirrus masks the more textured OT and prevents the matching process from producing a strong match.

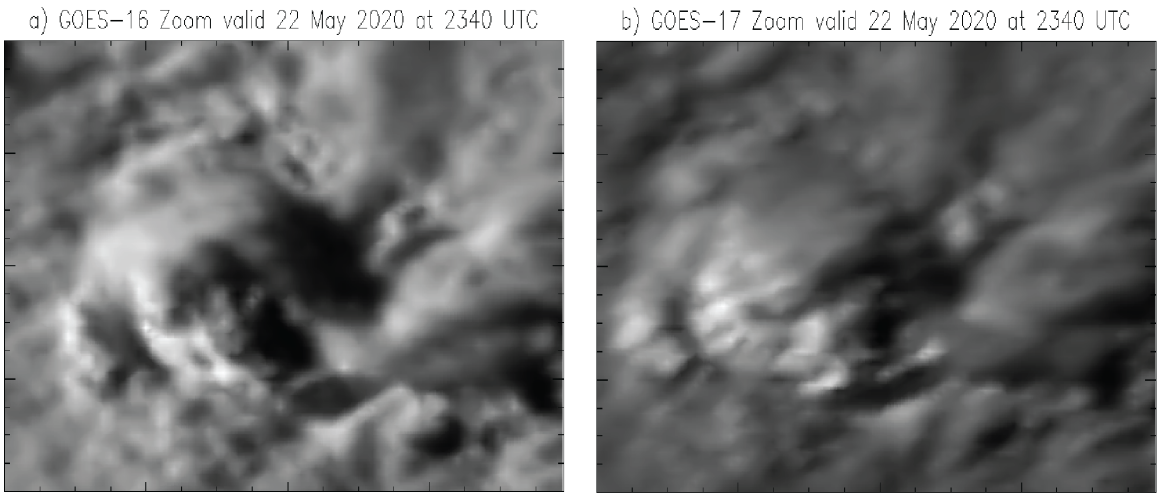

Figure 3.15: Zoom in of overshoot from a.) GOES-16 and b.) GOES-17 from 22 May 2020 valid at 2340 UTC.

Examples of cold CTTs not being well resolved from stereo are northwest of the west Texas storm on 13 May 2020 and on the eastern edge of storms on 8 June 2020. In both instances low level cirrus is advected from upstream into these regions which impairs the algorithms ability to create strong matches.

Chapter 4

Summary and Conclusions

In summary, using stereoscopy to determine CTHs from modern high-resolution visible imagery can yield heights comparable to echo top heights. While many prior studies have created methods of automated stereo, this study is the first to do so with 0.5 km visible imagery from GOES-16 and GOES-17. The stereo algorithm consists of 5 main steps; (1) preprocessing and regridding, (2) image matching, (3) iterative process, (4) quality control and filtering, and (5) converting to CTH. The stereo retrieved CTHs were then compared to echo top heights to assess the quality of CTH retrievals and the tropopause to determine when and where overshoots occurred. History maps of 6 severe weather events were shown side-by-side to compare echo tops, stereo CTHs, radar reflectivity, and minimum IR temperature. Contrasting maxima in echo top heights, maxima in CTHs, and minima in IR revealed that the stereo algorithm was not resolving the smaller scale features in overshoots and was therefore underestimating these regions. Analyzing time series of several storm tracks from 6 different cases revealed finer temporal scale events of interest. Two cases, 17 May 2019 and 23 April 2021, showed a spike in CTHs before tornadogenesis. These occurrences support the claims made by Adler and Fenn (1981) of CTHs increasing before a tornado forms.

The cases selected for this study present a couple caveats. Between the 6 cases there was not substantial diversity in convective mode. These cases featured either supercells or a broken line of storms. Including events such as large MCSs (e.g., derechos) or hurricanes would test the stereo algorithm further to see how it handles different cloud fields. A hurricane study with GOES-R imagery at 0.5 km could only be possible with a landfalling hurricane on the coast of Texas. This is because

the eastern extent of GOES-17 does not extend further east. Secondly, the sample size of cases is a caveat to this study. The small sample size is not large enough to draw definitive conclusions on many issues, but required substantial computational resources and relies on overlapping GOES-16 and GOES-17 mesoscale domains, which are rare (< 5 per year). It is hypothesized an increase in sample size could move results to having no bias instead of a low bias when compared to echo tops.

Future work utilizing stereoscopy to calculate CTHs with GOES can investigate the following to improve upon that done here. Perhaps the most significant concern is the inability for the algorithm to resolve and correctly place small scale features. The most likely reason for this is the difference in the scattering of light from the different viewpoints of GOES-16 and GOES-17. An algorithm which leverages multispectral data could be useful in overcoming this obstacle by capturing a more accurate depiction of the small cloud features. However, incorporating various data sets of coarser resolution results in a loss of the high resolution from visible imagery. A technique developed by Bedka and Khlopenkov (2016) uses visible cloud texture as an advantage to detect OTs. This method was proven to be 20% more accurate at detecting OTs than the best alternative existing method. The benefit of incorporating this technique into the stereo algorithm is preserving the native horizontal resolution of 0.5 km visible imagery and may be the most promising approach.

The data used as verification and to determine the quality of stereo retrieved CTHs were echo top heights from GridRad. The vertical resolution of GridRad data varies greatly by region, as shown in Figure 3.1, and by operating mode of the radar, the specifications of which have changed over the years. The most common volume coverage patterns (VCPs) when observing precipitation are VCP-11, VCP-12, and VCP-21. VCP-21 is used for shallower precipitation while VCP-11 and VCP-12 are used for convective precipitation. VCP-11 samples more at higher levels and VCP-12 samples more at lower levels. This difference in modes leads to more uncertainty at

higher altitudes in VCP-12 compared to VCP-11. More information on the different operating modes of WSR-88D radars can be found in OFCM (2017). Since GridRad has a large uncertainty in echo top heights, a different data source could be used for stereo CTH verification. Vertically pointing instruments on polar orbiting satellites from the A-train satellite constellation, specifically the CPR onboard the CloudSat satellite and the Cloud-Aerosol Lidar with Orthogonal Polarization (CALIOP) on the CALIPSO satellite, can be used to more accurately resolve CTHs. The vertical resolution of CPR is 480 m and 240 m with oversampling, and the vertical resolution of CALIOP is 30-60 m. CALIOP also features a finer horizontal resolution of 333 m compared to as coarse as 1.7 km from CPR. Setvák et al. (2013) compared data from several cases from the instruments aboard satellites from the A-train constellation. Comparison of CALIOP and CPR data revealed an important distinction between both instruments. A profile from CALIOP of an overshooting storm showed a higher cloud material in the overshooting region than CPR could detect. CALIOP was able to detect smaller ice particles in this feature while CPR could not (Setvák et al., 2013). Although these satellites would provide higher vertical resolution and a higher certainty of actual CTHs, this data is not regularly available because they are polar orbiting satellites and overpasses during the times of deep convective activity over land are very infrequent. Setvák et al. (2013) also argues the definition of CTHs is subjective to the instrument being used. The optical thickness of the cloud heavily influences the apparent CTH.

One of the motivations for this study was to create an algorithm capable of resolving CTHs near the core of a storm for use in an operational setting. Using two different search areas for the first iteration is problematic when applying this in an operational setting. Realistically, the search area would not have to be manually selected to achieve optimal results. A larger search area is required for higher CTHs. A proposed method for determining the proper search area incorporates the time of

year and the region of interest. Generally, a lower tropopause yields relatively lower CTHs and a higher tropopause allows for higher CTHs. Using a historical average of tropopause height based on region and time of year can help determine a preset search area based on these two factors. Alternatively, a search area can be determined in real-time based on the latest tropopause heights in the region of interest from the nearest sounding or other source. As mentioned previously, simply using a higher search area for the first iteration and implementing a harsher filter would erase the finer scale features that can be resolved using visible imagery with 0.5 km resolution.

Going forward, a successful stereo CTH retrieval algorithm can be used as another OT detection method for fine space and time scale analysis. Stereo only relies on geometric relationships of multi-satellite imagery and therefore does not have inevitable errors from methods that derive CTH from IR temperature alone. The indirect relationship of IR temperature and CTH will fail to accurately identify OTs in regions with an enhanced-V signature due to the relatively warm cloud tops above the tropopause and other similar scenarios. Finally, this stereo algorithm outputs CTH retrievals in the highest resolution possible from geostationary satellite imagery. While we expect this to result in a more accurate detection of OTs with a lower false detection rate, we found considerable underestimates of CTH in overshooting regions. This was due to the inability of the algorithm to resolve smaller features which can be the result of not a large enough initial search area, too harsh of a filter and smoothing applied, steep sloping cloud edges resulting in hard to match regions, or high level cirrus masking the higher texture cloud tops of the storm. Possible solutions to this include using IR imagery in later iterations or using the cloud texture algorithm described above to avoid poor matches from differences in appearance from visible imagery.

Bibliography

Adler, R. F. and D. D. Fenn, 1981: Satellite-observed cloud-top height changes in tornadic thunderstorms. *Journal of Applied Meteorology and Climatology*, **20 (11)**, 1369 – 1375, doi:10.1175/1520-0450(1981)020⟨1369:SOCTHC⟩2.0.CO;2.

Alberty, R. L., D. W. Burgess, C. E. Hane, and J. F. Weaver, 1979: Sesame 1979 operations summary, project severe environmental storms and mesoscale experiment. 253 pp.

Bedka, K., J. Brunner, R. Dworak, W. Feltz, J. Otkin, and T. Greenwald, 2010: Objective satellite-based detection of overshooting tops using infrared window channel brightness temperature gradients. *Journal of Applied Meteorology and Climatology*, **49 (2)**, 181 – 202, doi:10.1175/2009JAMC2286.1.

Bedka, K., E. M. Murillo, C. R. Homeyer, B. Scarino, and H. Mersiovsky, 2018: The above-anvil cirrus plume: An important severe weather indicator in visible and infrared satellite imagery. *Weather and Forecasting*, **33 (5)**, 1159 – 1181, doi:10.1175/WAF-D-18-0040.1.

Bedka, K. M. and K. Khlopenkov, 2016: A probabilistic multispectral pattern recognition method for detection of overshooting cloud tops using passive satellite imager observations. *Journal of Applied Meteorology and Climatology*, **55 (9)**, 1983 – 2005, doi:10.1175/JAMC-D-15-0249.1.

Bedka, K. M., C. Wang, R. Rogers, L. D. Carey, W. Feltz, and J. Kanak, 2015: Examining deep convective cloud evolution using total lightning, wsr-88d, and goes-14 super rapid scan datasets. *Weather and Forecasting*, **30 (3)**, 571 – 590, doi:10.1175/WAF-D-14-00062.1.

Berendes, T. A., J. R. Mecikalski, W. M. MacKenzie Jr., K. M. Bedka, and U. S. Nair, 2008: Convective cloud identification and classification in daytime satellite imagery using standard deviation limited adaptive clustering. *Journal of Geophysical Research: Atmospheres*, **113 (D20)**, doi:https://doi.org/10.1029/2008JD010287.

Bluestein, H. B., D. T. Lindsay, D. Bikos, and Z. B. Wienhoff, 2019: The relationship between overshooting tops in a tornadic supercell and its radar-observed evolution. *Monthly Weather Review*, **147 (1)**, 4151 – 4176, doi:10.1175/MWR-D-19-0159.1.

Cooney, J. W., K. P. Bowman, C. R. Homeyer, and T. M. Fenske, 2018: Ten year analysis of tropopause-overshooting convection using gridrad data. *Journal of Geophysical Research: Atmospheres*, **123 (1)**, 329–343, doi:https://doi.org/10.1002/2017JD027718.

Fujita, T. T., 1974: Overshooting thunderheads observed from ats and learjet. 1 – 227.

Fujita, T. T., 1982: Principle of stereoscopic height computations and their applications to stratospheric cirrus over severe thunderstorms. *Journal of the Meteorological Society of Japan*, **60 (1)**, 355 – 368.

Gelaro, R., et al., 2017: The modern-era retrospective analysis for research and applications, version 2 (merra-2). *Journal of Climate*, **30 (14)**, 5419 – 5454, doi:10.1175/JCLI-D-16-0758.1.

Gettelman, A., P. Hoor, L. L. Pan, W. J. Randel, M. I. Hegglin, and T. Birner, 2011: The extratropical upper troposphere and lower stratosphere. *Reviews of Geophysics*, **49 (3)**, doi:https://doi.org/10.1029/2011RG000355.

Griffin, S. M., K. M. Bedka, and C. S. Velden, 2016: A method for calculating the height of overshooting convective cloud tops using satellite-based ir imager and cloudsat cloud profiling radar observations. *Journal of Applied Meteorology and Climatology*, **55 (2)**, 479 – 491, doi:https://doi.org/10.1175/JAMC-D-15-0170.1.

Hasler, A., R. Mack, and A. Negri, 1983: Stereoscopic observations from meteorological satellites. *Advances in Space Research*, **2 (6)**, 105–113, doi:https://doi.org/10.1016/0273-1177(82)90130-2.

Hasler, A. F., 1981: Stereographic observations from geosynchronous satellites: An important new tool for the atmospheric sciences. *Bulletin of the American Meteorological Society*, **62 (2)**, 194 – 212, doi:10.1175/1520-0477(1981)062⟨0194:SOFGSA⟩2.0.CO;2.

Hasler, A. F., J. Strong, R. H. Woodward, and H. Pierce, 1991: Automatic analysis of stereoscopic satellite image pairs for determination of cloud-top height and structure. *Journal of Applied Meteorology and Climatology*, **30 (3)**, 257 – 281, doi:10.1175/1520-0450(1991)030⟨0257:AAOSSI⟩2.0.CO;2.

Holton, J. R., P. H. Haynes, M. E. McIntyre, A. R. Douglass, R. B. Rood, and L. Pfister, 1995: Stratosphere-troposphere exchange. *Reviews of Geophysics*, **33 (4)**, 403–439, doi:https://doi.org/10.1029/95RG02097.

Homeyer, C. R. and K. P. Bowman, 2017: Algorithm description document for version 3.1 of the three-dimensional gridded nexrad wsr-88d radar (gridrad) dataset.

Homeyer, C. R., J. D. McAuliffe, and K. M. Bedka, 2017: On the development of above-anvil cirrus plumes in extratropical convection. *Journal of the Atmospheric Sciences*, **74 (5)**, 1617 – 1633, doi:10.1175/JAS-D-16-0269.1.

Kassander, A. R. and L. L. Sims, 1957: Cloud photogrammetry with ground-located k-17 aerial cameras. *Journal of Atmospheric Sciences*, **14 (1)**, 43 – 49, doi:10.1175/0095-9634-14.1.43.

Kikuchi, K. and T. Kasai, 1968: Stereoscopic analysis of photographs taken by nimbus ii apt system. *Journal of the Meteorological Society of Japan. Ser. II*, **46 (1)**, 60–67, doi:10.2151/jmsj1965.46.1_60.

Lee, J., D.-B. Shin, C.-Y. Chung, and J. Kim, 2020: A cloud top-height retrieval algorithm using simultaneous observations from the himawari-8 and fy-2e satellites. *Remote Sensing*, **12 (12)**, doi:10.3390/rs12121953.

Lindsey, D. T. and L. Grasso, 2008: An effective radius retrieval for thick ice clouds using goes. *Journal of Applied Meteorology and Climatology*, **47 (4)**, 1222 – 1231, doi:10.1175/2007JAMC1612.1.

Meyer, H., 1954: Wolken photogrammetrie mit einfachen hilfsmitteln. *Bildmessung u. Luftbildwesen*, **22**, 9–15.

Minzner, R. A., W. E. Shenk, R. D. Teagle, and J. Steranka, 1978: Stereographic cloud heights from imagery of sms/goes satellites. *Geophysical Research Letters*, **5 (1)**, 21–24, doi:https://doi.org/10.1029/GL005i001p00021.

NOAA, 1994: Noaa geostationary operational environmental satellite imager data. noaa comprehensive large array- data stewardship system.

OFCM, 2017: Federal meterological handbook no. 11 – wsr-88d meteorological observations, part c: Wsr-88d products and algorithms. fcm-h11c-2017.

Ondrejka, R. J. and J. H. Conover, 1966: Note on the stereo interpretation of nimbus ii apt photography. *Monthly Weather Review*, **94 (10)**, 611 – 614, doi:10.1175/1520-0493(1966)094⟨0611:NOTSIO⟩2.3.CO;2.

Roach, W. T., 1967: On the nature of the summit areas of severe storms in oklahoma. *Quarterly Journal of the Royal Meteorological Society*, **93 (397)**, 318–336, doi:https://doi.org/10.1002/qj.49709339704.

Rosenfeld, D., W. L. Woodley, A. Lerner, G. Kelman, and D. T. Lindsey, 2008: Satellite detection of severe convective storms by their retrieved vertical profiles of cloud particle effective radius and thermodynamic phase. *Journal of Geophysical Research: Atmospheres*, **113 (D4)**, doi:https://doi.org/10.1029/2007JD008600.

Sandmæl, T. N., 2017: An evaluation of radar and satellite data based products to discriminate between tornadic and non-tornadic storms. M.S. thesis, School of Meteorology, University of Oklahoma.

Sandmæl, T. N., C. R. Homeyer, K. M. Bedka, J. M. Apke, J. R. Mecikalski, and K. Khlopenkov, 2019: Evaluating the ability of remote sensing observations to identify significantly severe and potentially tornadic storms. *Journal of Applied Meteorology and Climatology*, **58 (12)**, 2569 – 2590, doi:10.1175/JAMC-D-18-0241.1.

Schmit, T., M. Gunshor, G. Fu, T. Rink, K. Bah, W. Zhang, and W. Wolf, 2012: Goes-r advanced baseline imager (abi) algorithm theoretical basis document for cloud and moisture imagery product (cmip).

Seiz, G., S. Tjemkes, and P. Watts, 2007: Multiview cloud-top height and wind retrieval with photogrammetric methods: Application to meteosat-8 hrv observations. *Journal of Applied Meteorology and Climatology*, **46 (8)**, 1182 – 1195, doi:10.1175/JAM2532.1.

Setvák, M., K. Bedka, D. T. Lindsey, A. Sokol, Z. Charvát, J. Šťástka, and P. K. Wang, 2013: A-train observations of deep convective storm tops. *Atmospheric Research*, **123**, 229–248, doi:https://doi.org/10.1016/j.atmosres.2012.06.020, 6th European Conference on Severe Storms 2011. Palma de Mallorca, Spain.

Shenk, W. E., R. J. Holub, and R. A. Neff, 1975: Stereographic cloud analysis from apollo 6 photographs over a cold front. *Bulletin of the American Meteorological Society*, **56 (1)**, 4 – 16, doi:10.1175/1520-0477-56.1.4.

Solomon, D. L., K. P. Bowman, and C. R. Homeyer, 2016: Tropopause-penetrating convection from three-dimensional gridded nexrad data. *Journal of Applied Meteorology and Climatology*, **55 (2)**, 465 – 478, doi:10.1175/JAMC-D-15-0190.1.

Stohl, A., et al., 2003: Stratosphere-troposphere exchange: A review, and what we have learned from staccato. *Journal of Geophysical Research: Atmospheres*, **108 (D12)**, doi:https://doi.org/10.1029/2002JD002490.

WMO, 1957: Definition of the tropopause. *WMO Bull.*, **6**, 136.

Xian, T. and C. R. Homeyer, 2019: Global tropopause altitudes in radiosondes and reanalyses. *Atmospheric Chemistry and Physics*, **19 (8)**, 5661–5678, doi:10.5194/acp-19-5661-2019.